Bioorganic Chemistry 110 (2021) 104748

Contents lists available at ScienceDirect

Bioorganic Chemistry

journal homepage: www.elsevier.com/locate/bioorg

Development of isatin-thiazolo[3,2-*a*]benzimidazole hybrids as novel CDK2 inhibitors with potent *in vitro* apoptotic anti-proliferative activity: Synthesis, biological and molecular dynamics investigations

Wagdy M. Eldehna [a,*], Mahmoud A. El Hassab [b], Mahmoud F. Abo-Ashour [c], Tarfah Al-Warhi [d], Mahmoud M. Elaasser [e], Nesreen A. Safwat [e], Howayda Suliman [f], Marwa F. Ahmed [g,h], Sara T. Al-Rashood [i], Hatem A. Abdel-Aziz [j], Radwan El-Haggar [g]

[a] *Department of Pharmaceutical Chemistry, Faculty of Pharmacy, Kafrelsheikh University, Kafrelsheikh P.O. Box 33516, Egypt*
[b] *Department of Pharmaceutical Chemistry, School of Pharmacy, Badr University in Cairo, Badr City 11829, Cairo, Egypt*
[c] *Department of Pharmaceutical Chemistry, Faculty of Pharmacy, Egyptian Russian University, Badr City, Cairo, Egypt*
[d] *Department of Chemistry, College of Science, Princess Nourah bint Abdulrahman University, Riyadh, Saudi Arabia*
[e] *The Regional Center for Mycology and Biotechnology, Al-Azhar University, Cairo, Egypt*
[f] *Department of Medical Biochemistry, Faculty of Medicine, Alexandria University, Alexandria, Egypt*
[g] *Pharmaceutical Chemistry Department, Faculty of Pharmacy, Helwan University, 11795 Cairo, Egypt*
[h] *Department of Pharmaceutical Chemistry, Faculty of Pharmacy, Taif University, Taif 21974, Saudi Arabia*
[i] *Department of Pharmaceutical Chemistry, College of Pharmacy, King Saud University, P.O. Box 2457, Riyadh 11451, Saudi Arabia*
[j] *Department of Applied Organic Chemistry, National Research Center, Dokki, Giza P.O. Box 12622, Egypt*

ARTICLE INFO

Keywords:
Anticancer
CDK2 inhibitors
Indolin-2-one
Thiazolobenzimidazole
Molecular docking
Molecular dynamics

ABSTRACT

In the current medical era, human health is experiencing numerous challenges, particularly the human malignancies. Therefore, the therapeutic arsenal for these malignancies is to be inexorably enhanced with new treatments that target tumor cells in a selective manner. In this regard, the present work aims at developing a new set of small molecules featuring the privileged isatin scaffold conjugated with a thiazolo[3,2-*a*]benzimidazole (**TBI**) motif through a cleavable hydrazide linker (**7a-e** and **10a-i**) as potential anticancer CDK2 inhibitors. The large tricyclic **TBI** motif is anticipated to achieve a plethora of hydrophobic interactions within the CDK2 binding site. The growth of the two examined cell lines was significantly inhibited by most the prepared hybrids with IC_{50} ranges; (2.60 ± 1.47–20.90 ± 1.17 μM, against MDA-MB-231) and (1.27 ± 0.06–16.83 ± 0.95 μM, against MCF-7). In particular, hybrids **7a**, **7d** and **10a** displayed potent dual activity against the examined cell lines, and thus selected for further investigations. They exerted a significance alteration in the cell cycle progression, in addition to an apoptosis induction within both MDA-MB-231 and MCF-7 cells. Furthermore, **7a**, **7d** and **10a** displayed potent CDK2 inhibitory action (IC_{50} = 96.46 ± 5.3, 26.24 ± 1.4 and 42.95 ± 2.3 nM, respectively). The docking simulations unveiled, as expected, the ability of the TBI ring to well-accommodate and establish several hydrophobic interactions within a hydrophobic pocket in the CDK2 binding site. Also, the docking simulations highlighted the significance of incorporation of the hydrazide linker and isatin unsubstituted (NH) functionality in the H-bonding interactions. Interestingly, the most potent CDK2 inhibitor **7d** achieved the best binding score (-11.2 Kcal/mole) and formed the most stable complex with CDK2 enzyme (RMSD = 1.24 Å) in a 100 ns MD simulation. In addition, the MM-PBSA calculations ascribed the lowest binding free energy to the **7d**–CDK2 complex (−323.69 ± 15.17 kJ/mol). This could be attributed to an incorporation of the 5-OCH_3 group that was engaged in an extra hydrogen bonding with key THR14 amino acid residue. Finally, these results suggested hybrid **7d** as a good candidate for further optimization as promising breast cancer antitumor agent and CDK2 inhibitor.

* Corresponding author.
E-mail addresses: wagdy2000@gmail.com, wagdy.mohamad@pharm.kfs.edu.eg (W.M. Eldehna).

https://doi.org/10.1016/j.bioorg.2021.104748
Received 27 August 2020; Received in revised form 9 December 2020; Accepted 13 February 2021
Available online 18 February 2021

1. Introduction

Cancer is one of the major global health problems, characterized by rapid and uncontrolled cell proliferation [1], and still considered a major cause of death worldwide [2]. The early cancer treatment strategies were based on the unspecific death induction in replicating cells that mainly targeting the DNA synthesis [3–5] and the replication machinery [6–9]. These traditional cytotoxic chemotherapies were associated with significant adverse effects due to the nature of the treatment in addition to the resistance developed toward them [10]. So, the search for new effective and safe anticancer agents with increased selectivity toward cancer cells is still a crucial need [11,12]. In this respect, the more recent strategies (the targeted therapies) aim to identify and target specific biomarkers fundamental for cancer cells such as deregulated, mutated, or overexpressed proteins [13]. In recent past, protein kinases represented important molecular targets for the development of novel anticancer agents and in this manner numerous kinase inhibitors are already in the clinical use and trials [14,15].

Cyclin-dependent kinases (CDKs) are family of threonine-serine protein kinases that regulate fundamental cellular processes, such as gene transcription, cell cycle progression and cell division [16,17]. In mammalian cells, the CDK family consisted of 20 members (CDK1-20) where their cellular functions are activated by association of CDK with corresponding regulatory protein subunits named cyclins. The human genome encodes 29 cyclins which form active complexes with their CDK partners [18–22]. In this manner, CDK2, one significant member of CDKs family, complexed with cyclin E enables retinoblastoma protein (pRb) phosphorylation, and activation of transcription factors E2F that promotes the cell cycle transition from G1 to S phase [23]. In addition, CDK2 complexed with cyclinA, promotes continuous DNA replication and properly programmed deactivation of E2F. Thus, CDK2 has become a significant drug target for the treatment of cancer [18]. Recently, CDK2 inhibitors evidenced as therapeutic targets in ovarian cancer [24], neuroblastoma [25] and BRCA-deficient cancers [26]. In addition, several CDK2 inhibitors had been developed and some of them introduced to clinical evaluation (roscovitine, CYC065, dinaciclib, AT7519, milciclib) [27,28].

Isatin (1*H*-indole-2,3-dione), as an important privileged scaffold in medicinal chemistry, represents a leading and promising heterocyclic nucleus that is included in many small molecules possessing a wide range of interesting biological activities such as antimicrobial, antiviral, anticonvulsant and many other activities [29–38], with a great interest of the development of efficient isatin-based anticancer agents [39–41] such as Semaxanib, Sunitinib, and Nintedanib (Fig. 1) [42].

In this respect, many isatin-based derivatives were reported as potential inhibitors for several tyrosine and serine/threonine kinases such as CDKs [43,44]. In addition, several isatin hybrids were reported for their promising anticancer activities [45–47].

Our research group, in the current year, has reported three studies concerning the development of diverse series of isatin-based anticancer candidates with potential CDK2 inhibitory activity [48–50]. In these studies, the isatin scaffold was conjugated to an indol-2-yl motif through a hydarzide linker (Compound **I**, Fig. 1), as well as it was conjugated to an indol-3-yl motif through acetohydrazide or hydrazone linkers

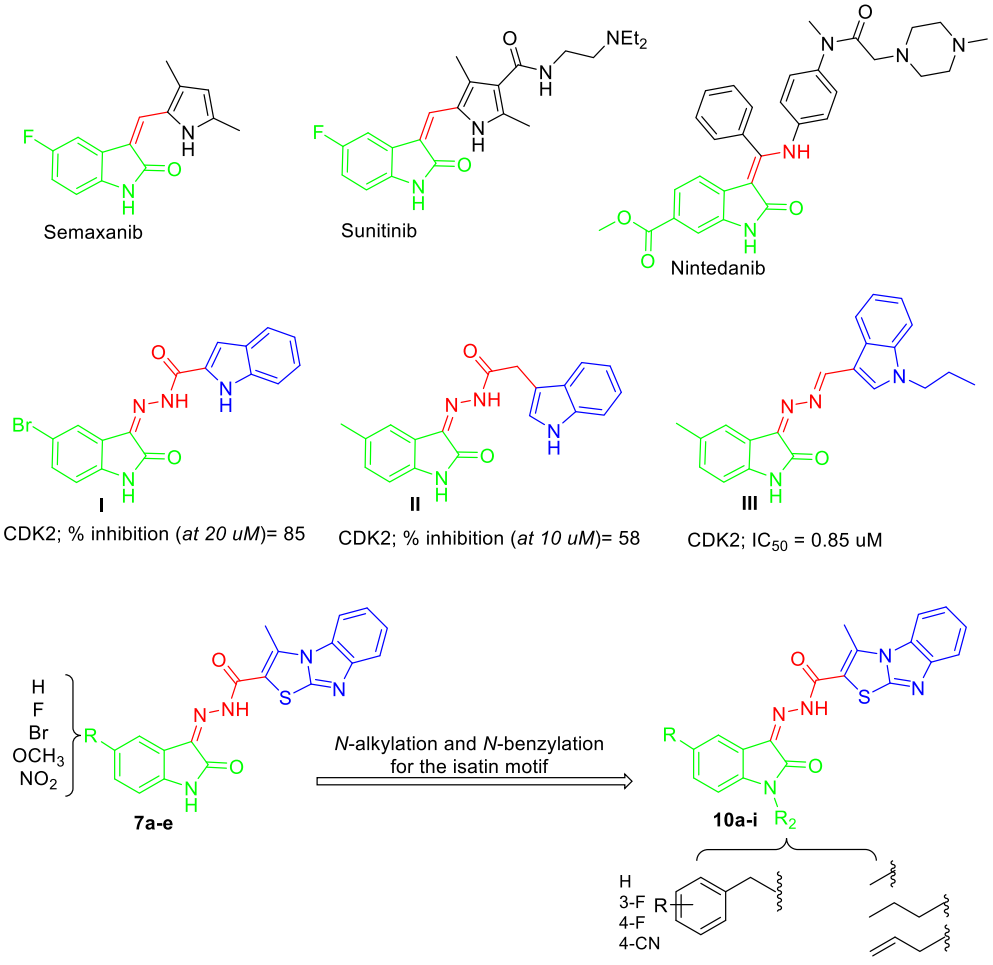

Fig. 1. Chemical structures for isatin-based anticancer agents (Semaxanib, Sunitinib, and Nintedanib), reported isatin-based anticancer CDK2 inhibitors (**I**–**III**), and target hybrids (**7a-e** and **10a-i**).

(Compounds **II** and **III**, respectively, Fig. 1). The results obtained from these three studies ascribed to the developed isatin-based conjugates **I** and **II** moderate inhibitory activity toward CDK2 (85% inhibition at 20 μM and 58% inhibition at 10 μM, respectively). Worthy of note, conjugation of isatin scaffold with the more lipophilic *N*-propyl-indole moiety in compound **III**, than *N*-unsubstituted indole moieties in compounds **I** and **II**, resulted in the best inhibitory activity (compound **III**; $IC_{50} = 0.85$ μM, Fig. 1). This could be attributed to the ability of compound **III** to achieve more hydrophobic interactions than compounds **I** and **II** within the hydrophobic CDK2 binding site.

On the other hand, thiazolo[3,2-*a*]benzimidazole (TBI) is considered a scaffold of interest in the field of medicinal and pharmaceutical chemistry with diverse biological properties especially anticancer activities[51–53].

In the light of all the findings mentioned above, and as part of our ongoing endeavor to develop novel oxindole-based anticancer candidates targeting CDK2 [48–50], this study was devoted to develop a new set of small molecules featuring oxindole scaffold conjugated with a thiazolo[3,2-*a*]benzimidazole (TBI) motif through a cleavable flexible hydrazide linker (**7a-e** and **10a-i**, Fig. 1) as potential anticancer CDK2 inhibitors. In this study, the indole moiety in the previously reported oxindole-based derivatives (**I-III**, Fig. 1) was replaced with a TBI one, exploiting a bioisosteric replacement approach. The large tricyclic TBI motif is anticipated to achieve a plethora of hydrophobic and Van der Waals interactions within the hydrophobic CDK2 binding site [54], whereas, the TBI sp^2 nitrogen is expected to engage a hydrogen bond within the CDK2 active site.

All the herein newly synthesized isatin-TBI hybrids (**7a-e** and **10a-i**) were screened for their anti-proliferation activity against two cancer cell lines; MDA-MB-231 and MCF-7. Then, the most promising analogues, in the cytotoxic assay, were evaluated for their activity against CDK2, as well as their impact on cell cycle progression and provoke of apoptosis were explored.

2. Results and discussion

2.1. Chemistry

The synthetic strategies deliberated for preparation of the novel isatin-TBI hybrids (**7a-e** and **10a-i**) were illustrated in Schemes 1–2. In Scheme 1, 1*H*-benzimidazole-2-thiol **1** was reacted with ethyl 2-chloro-3-oxobutanoate **2** in absolute ethanol to furnish intermediate **3**, which then heterocyclized to ethyl 3-methylbenzo[4,5]imidazo[2,1-*b*]thiazole-2-carboxylate **4** via heating under reflux in acetic anhydride. The ester analogue **4** was subjected to hydrazinolysis to produce the key intermediate hydrazide **5**, which condensed with different isatin moieties (**6a-e**) in glacial acetic acid to give the targeted hybrids **7a-e**.

On the other hand, isatin **6a** and 5-bromoisatin **6c** were *N*-alkylated with different alkyl halides **8a-g** in anhydrous DMF to furnish *N*-substituted isatins **9a-i** that thereafter condensed with the hydrazide intermediate **5** in glacial acetic acid to produce the final novel compounds **10a-i** (Scheme 2).

The proposed novel isatin-TBI hybrids **7a-e** and **10a-i** were in full agreement with the obtained spectral and elemental analyses data. ^{1}H NMR spectra for all herein reported new compounds (**7a-e** and **10a-i**) identified the presence of two singlet signals for protons of the C-3 methyl group and NH functionality of the hydrazide linker at range δ 3.22–3.23 *ppm* and 11.99–13.10 *ppm*, respectively. In addition, the structure of compounds **7a-e** was confirmed with presence of another singlet signal for NH of isatin moiety at range δ 11.02–11.85 *ppm*. Moreover, ^{1}H NMR spectra for compounds **10d-g** and **10i** revealed the presence of benzylic protons at range δ 4.99–5.05 *ppm*, whereas, ^{1}H NMR spectra for compounds **10b** and **10 h** showed two triplet peaks for —CH_2—CH_3 and *N*-CH_2 around δ 0.90 and 3.71 *ppm*, respectively, in addition to a multiplet peak assigned for —CH_2—CH_3 protons at δ 1.69 and 1.66 *ppm*, respectively.

On the other hand, ^{13}C NMR spectra for target hybrids (**7a, 7b, 10a, 10b, 10d, 10f,** and **10 g**) displayed the signals attributable for the carbons of C-3 methyl group, C═O of the isatin moiety, and C═O of the hydrazide linker at range δ 14.17–21.50 *ppm*, 159.86–163.09 *ppm* and 168.96–172.74 *ppm*, respectively. In addition, the benzylic carbons of compounds **10d-g** and **10i were** identified at range δ 41.83–46.45 *ppm*.

2.2. Biological evaluation

2.2.1. Anti-proliferative activity towards breast MDA-MB-231 and MCF-7 cancer cell lines

All of the newly herein synthesized isatin-TBI hybrids (**7a–e** and **10a–i**) were screened for their potential anti-proliferation activity towards MDA-MB-231 and MCF-7 breast cancer cell lines, using the procedure of the Sulforhodamine B colorimetric (SRB) assay [55]. Staurosporine, an anticancer agent, was used as a positive control drug and the results have been reported as IC_{50} values and showed in Table 1.

Analyzing the results towards MDA-MB-231 cell line revealed that all of the *N*-unsubstituted isatin-TBI series **7a-e** possessed excellent cytotoxic activity with single digit micromolar IC_{50} values (IC_{50} range: 3.30 ± 0.21–8.62 ± 0.51 μM), with an exception for 5-F substituted hybrid **7b** (IC_{50} = 42.64 ± 2.9 μM). In particular, 5-OCH_3 substituted hybrid **7d**

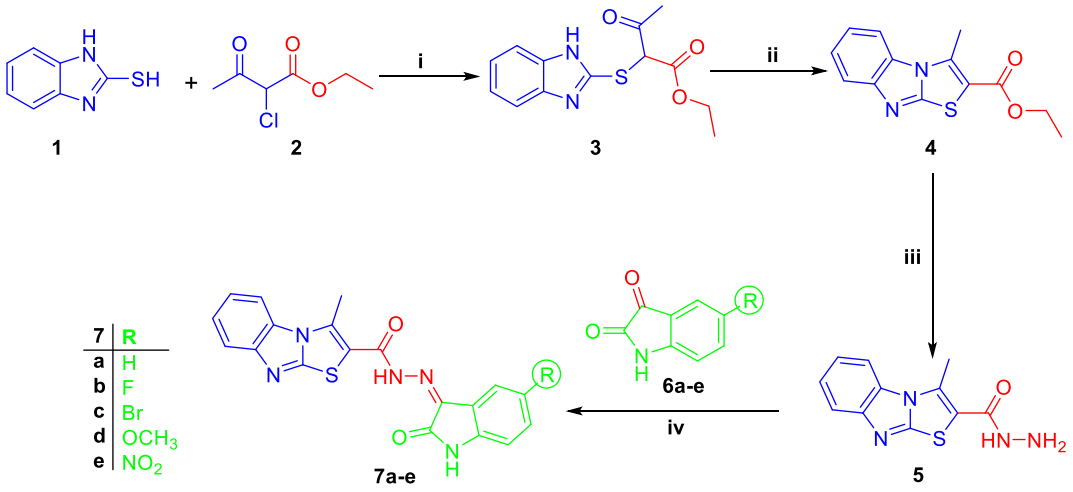

Scheme 1. Synthesis of target isatin-TBI hybrids **7a-e**; Reagents and conditions: (**i**) Abs. EtOH / TEA / reflux 6 h/(yield = 75%),(**ii**) Acetic anhydride / reflux 5 h/ (yield = 83%), (**iii**) hydrazine hydrate / isopropyl alcohol / reflux 6 h/ (yield = 88%), (**iv**) Glacial acetic acid / reflux 3–5 h / (yield: 72–84%).

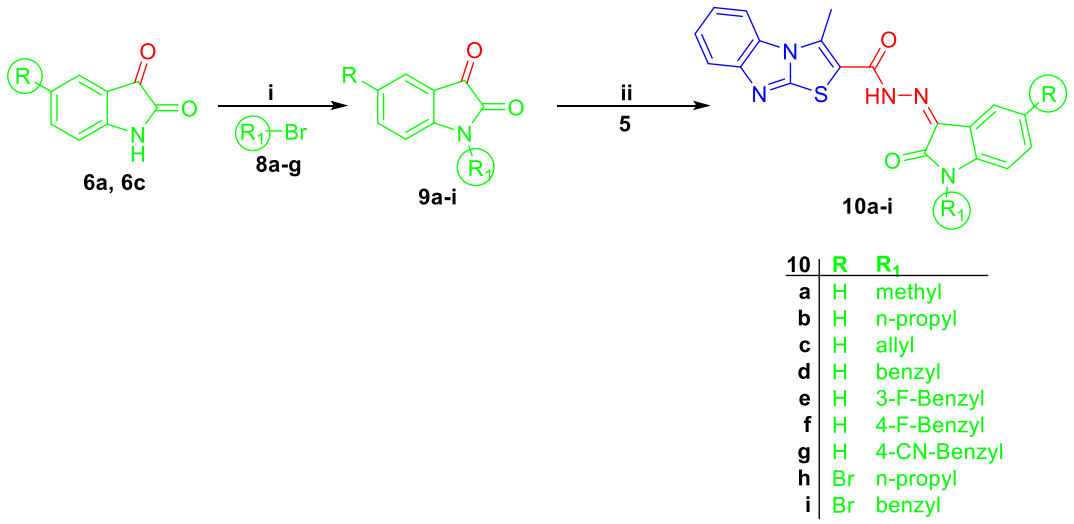

Scheme 2. Synthesis of *N*-substituted isatin-TBI hybrids **10a-i**; Reagents and conditions: (**i**) Anhydrous DMF / K_2CO_3 / reflux 4 h/ (yield: 70–85%) (**ii**) Glacial acetic acid / reflux 3–5 h/ (yield: 68–86%).

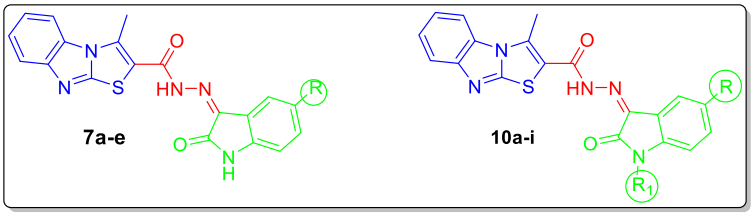

was the most active derivative with IC_{50} = 3.30 ± 0.21 μM which was comparable to Staurosporine that displayed IC_{50} equals 4.29 ± 0.72 μM, whereas, other isatin-TBI hybrids (**7a**, **7c** and **7e**) showed significant cytotoxicity activity with IC_{50} = 6.50 ± 0.32, 8.62 ± 0.51 and 8.11 ± 0.33 μM, respectively.

In a similar fashion, the results towards MCF-7 cell line showed that all *N*-unsubstituted isatin-TBI hybrids **7a-e** displayed potent anti-proliferative activity with single digit micromolar IC_{50} (IC_{50} range: 2.02 ± 0.13–9.39 ± 0.62 μM), with the exception of the same compound, **7b** (IC_{50} = 16.83 ± 0.95 μM). With aforementioned cell line, the unsubstituted hybrid **7a** was the most active counterpart (IC_{50} = 2.02 ± 0.13 μM) in this study with potency comparable to the utilized reference Staurosporine (IC_{50} = 3.81 ± 0.22 μM). Moreover, hybrids **7c**, **7d** and **7e**, showed excellent cytotoxic activity with IC_{50} = 9.39 ± 0.62, 5.82 ± 0.32 and 6.32 ± 0.48 μM, respectively (Table 1).

On the other hand, exploring the anticancer activities of the *N*-substituted isatin-TBI hybrids series **10a-i** towards MDA-MB-231 cell line revealed that *N*-substitution with only methyl (**10a**; IC_{50} = 2.60 ± 1.47), *N*-benzyl (**10d**; IC_{50} = 5.45 ± 0.28 μM) and 4-F-benzyl group (**10f**; IC_{50} = 7.65 ± 0.26 μM) maintained the activity, compared to the unsubstituted analog **7a** (IC_{50} = 6.50 ± 0.32 μM). Whereas, *N*-substitution with the *N*-ally (**10c**), *N*-propyl (**10b**) and *N*-4-CN-benzyl (**10g**) decreased the cytotoxic activity with IC_{50} = 13.73 ± 1.26, 18.06 ± 1.58, 20.90 ± 1.17 μM, respectively.

In addition, the *N*-substituted (**10h**) and (**10i**) showed different

Table 1
In vitro anti-proliferative activity of compounds**7a-e** and **10a-i** against breast MDA-MB-231 and MCF-7 cancer cell lines.

Comp.	R	R_1	IC_{50} (μM)[a]	
			MDA-MB-231	MCF-7
7a	H	–	6.50 ± 0.32	2.02 ± 0.13
7b	F	–	42.64 ± 2.9	16.83 ± 0.95
7c	Br	–	8.62 ± 0.51	9.39 ± 0.62
7d	OCH_3	–	3.30 ± 0.21	5.82 ± 0.32
7e	NO_2	–	8.11 ± 0.33	6.32 ± 0.48
10a	H	methyl	2.60 ± 1.47	3.01 ± 0.22
10b	H	n-propyl	18.06 ± 1.58	9.80 ± 0.67
10c	H	allyl	13.73 ± 1.26	1.27 ± 0.06
10d	H	benzyl	5.45 ± 0.28	6.66 ± 0.43
10e	H	3-F-benzyl	15.89 ± 2.03	3.37 ± 0.05
10f	H	4-F-benzyl	7.65 ± 0.26	26.02 ± 1.52
10g	H	4-CN-benzyl	20.90 ± 1.17	7.38 ± 0.34
10h	Br	n-propyl	4.77 ± 0.23	5.88 ± 0.29
10i	Br	benzyl	20.34 ± 1.67	10.33 ± 0.66
Staurosporine			4.29 ± 0.72	3.81 ± 0.22

[a] IC_{50} values are the mean ± S.D. of triplicate experiments.

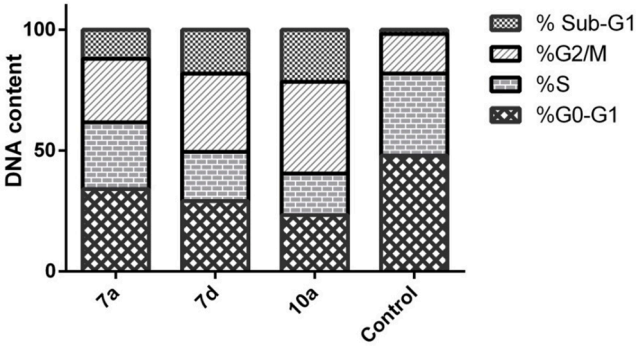

Fig. 2. Effect of isatin-TBI hybrids **7a**, **7d** and **10a** on the phases of cell cycle of MDA-MB-231 cells.

cytotoxic effect towards MDA-MB-231 cell line compared to the *N*-unsubstituted analog **7c** (IC_{50} = 8.62 ± 0.51 μM); while the *N*-propyl substitution (**10h**) enhanced the potency (IC_{50} = 4.77 ± 0.23 μM), the *N*-benzyl (**10i**) decreased the potency (IC_{50} = 20.34 ± 1.67 μM). Furthermore, the anti-proliferative activities of the *N*-substituted oxindole series **10a–i** towards MCF-7 cell line revealed that only *N*-allyl (**10c**) maintained the activity compared to the unsubstituted analog **7a** (IC_{50} = 2.02 ± 0.13 μM) while the remaining derivatives decreased the activity with IC_{50} ranged from 3.01 ± 0.22 μM to 26.02 ± 1.52 μM (Table 1).

2.2.2. Cell cycle analysis

It is well known that most of the cytotoxic compounds exert their anti-proliferative effect *via* arresting the cell cycle at certain phase. In this study, we examined the effect of the most potent isatin-TBI hybrids (**7a**, **7d** and **10a**) on cell cycle progression in order to define the phase at which cell cycle arrest takes place in both MDA-MB-231 and MCF-7 breast cancer cell lines. The effect on the cell cycle distribution was assessed by a DNA flow cytometry analysis, upon incubation of MDA-MB-231 and MCF-7 cells with isatin-TBI hybrids **7a**, **7d** and **10a** at theirIC_{50} concentrations for 24 h. As shown in the results, (Fig. 2), treatment of MDA-MB-231 cells with **7a**, **7d** and **10a** resulted in significant decrease in the cell population at the G0/G1 phase from 47.87% for the untreated control to 34.01%, 29.14% and 23.35%, respectively, for the treated cells (Fig. 2). In addition, hybrids **7a**, **7d** and **10a** resulted in an increase of G2/M phase by 1.6-, 2.0- and 2.3-fold, respectively, with concomitant elevation in the sub-G1 phase by 6.9-, 10.4- and 12.7-fold, respectively, in comparison to the control (Fig. 2).

Similarly, treatment of MCF-7 cells with the most active hybrids **7a**, **7d** and **10a** resulted in significant decrease in the percentage cell population at the G0/G1 phase to 19.94%, 33.53% and 24.94%, respectively, compared to that of the untreated control cells, which was 48.77% (Fig. 3). Also, hybrids **7a**, **7d** and **10a** resulted in a significant increase of the proportion of cells in the G2/M phase by 2.5-, 1.8- and 2.4-fold, respectively, in addition to elevation in the sub-G1 phase by 15.8-, 9.9- and 12.6-fold, respectively, in comparison to the control (Fig. 3). This upsurge of populations in the sub-G1 phase along with the arrest of G2-M phase were significant remarks for compounds **7a**, **7d** and **10a** to induce apoptosis in both MDA-MB-231 and MCF-7cell lines.

2.2.3. Apoptosis assay

Apoptosis as a major mechanism of the programmed cell death plays an important role in cancer metastasis [56–58]. Thus, apoptosis induction is considered as one of the main strategies for the development of anticancer agents [59]. In this study, the potential role of apoptosis in arresting the breast cancer (MDA-MB-231 and MCF-7) cells, when treated with the newly synthesized isatin-TBI hybrids, was assessed. Cells were treated with isatin-TBI hybrids **7a**, **7d** and **10a** then stained with Annexin V-FITC/PI.

As presented in Fig. 4, dual staining with Annexin-V and propidium iodide (PI) revealed that MDA-MB-231 cell underwent both early apoptosis (annexin-V^+/PI^-, lower right quadrant) and late apoptosis (annexin-V^+/PI^+, upper right quadrant). Significantly, the percent of early stage was increased from 0.62% of the control cells to 6.92%, 11.25% and 8.52% of cells incubated with hybrids **7a**, **7d** and **10a**, respectively. Also, the percent of late stage was increased from 0.39% of the control cells to 5.14%, 8.82% and 16.49% of cells treated with compounds **7a**, **7d** and **10a**, respectively. These indicated that compounds **7a**, **7d** and **10a** were able to induce an approximately 11.9-, 19.9- and 24.8-folds total increase in apoptosis, respectively, compared to the control for MDA-MB-231cell line.

On the other hands, results presented in Fig. 5, showed that MCF-7 cells incubated with hybrids **7a**, **7d** and **10a** displayed a significant increase of the percent of early apoptosis from 0.54% of the control cells to 6.99%, 4.82% and 8.31% of cells treated with hybrids **7a**, **7d** and **10a**, respectively. Also, the percent of late apoptosis was increased to 22.17%, 10.33% and 14.46% of cells treated with hybrids **7a**, **7d** and **10a**, respectively, compared to 0.37% of the control cells. These illustrated that the examined hybrids **7a**, **7d** and **10a** were able to increase the percent of total apoptosis by approximately 32.0-, 16.6- and 25.0-fold, respectively, compared to the control for MCF-7cells. In a word, the obtained results showed that the tested hybrids **7a**, **7d** and **10a** were significantly able to induce both early and late apoptosis stages in both MDA-MB-231 and MCF-7 breast cancer cell lines.

2.2.4. CDK2 inhibitory activity

The excellent *in vitro* anti-proliferative effects of isatin-TBI hybrids **7a**, **7d** and **10a** against both MDA-MB-231 and MCF-7 cell lines, in addition to their induction of apoptosis, motivated a further exploration for their possible inhibitory activity against the cell cycle regulator CDK2 protein kinase.

The results presented in Table 2 showed that 5-OCH_3 substituted hybrid **7d** was the most potent derivative with IC_{50} value of 26.24 nM that was superior to Staurosporine which exhibited IC_{50} value of 38.5 nM, followed by hybrids **10a** and **7a** with IC_{50} value of 42.95 and 96.46 nM, respectively.

2.3. In silico study

2.3.1. In silico ADME calculations

Compounds are considered potential candidates for drug discovery when they achieve a desired biological activity alongside with acceptable pharmacokinetic profiles. Thus, both the pharmacodynamics and pharmacokinetic profiles were taken in our perspective point of view when judging the potentiality of the three candidate hybrids**7a**, **7d** and **10a**. The SwissADME online tool created by the Swiss Institute of Bioinformatics (**SIB**) in order to calculate the ADME profiles and drug-like nature of the three lead hybrids. They all were predicted to have high

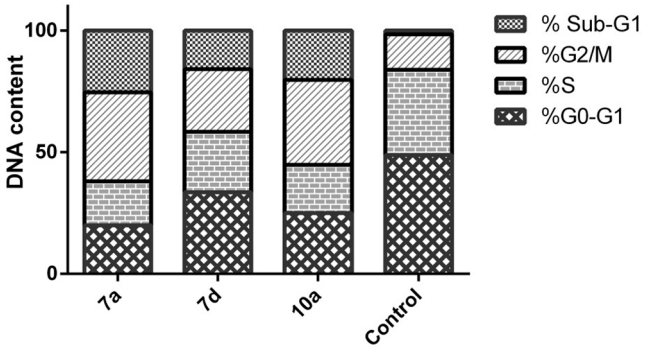

Fig. 3. Effect of isatin-TBI hybrids **7a**, **7d** and **10a** on the phases of cell cycle of MCF-7 cells.

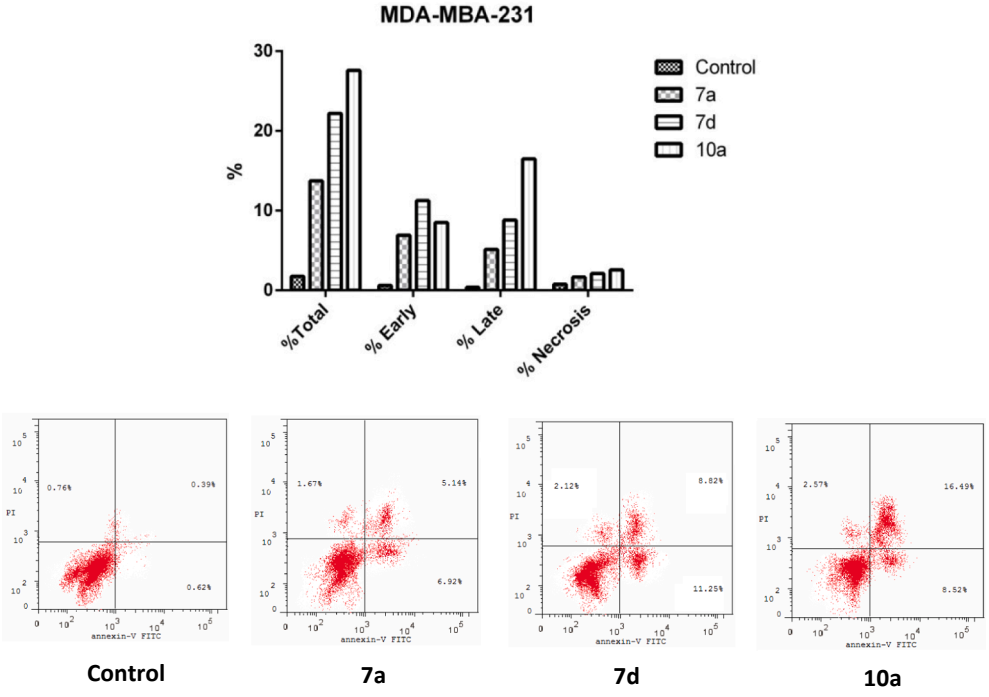

Fig. 4. Effect of hybrids **7a**, **7d** and **10a** on the percentage of annexin V-FITC-positive staining in MDA-MB-231 cells. The experiments were done in triplicates.

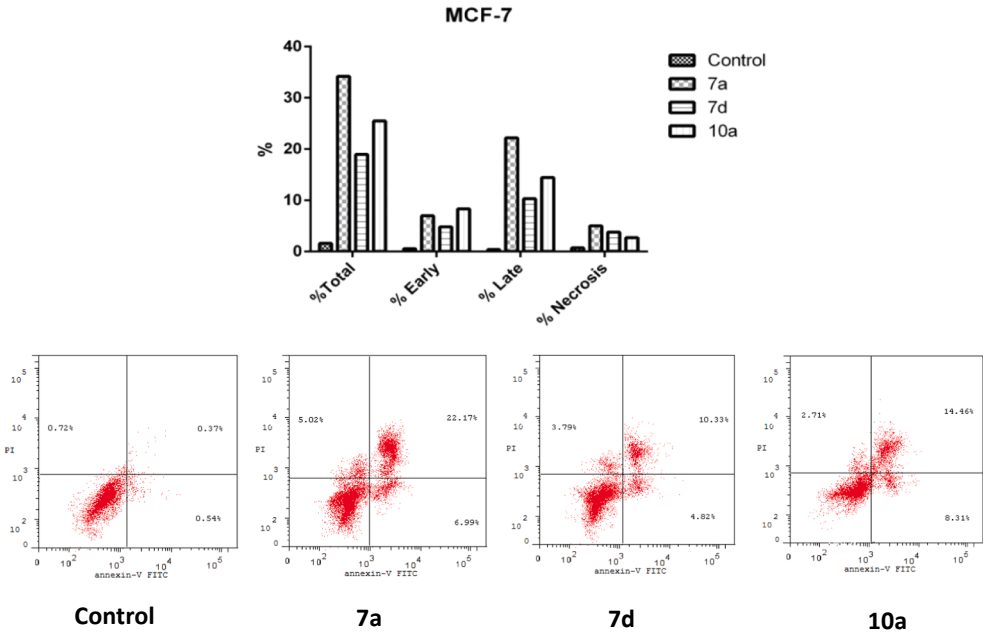

Fig. 5. Effect of **7a**, **7d** and **10a** on the percentage of annexin V-FITC-positive staining in MCF-7 cells. The experiments were done in triplicates.

Table 2
Inhibitory activity of isatin-TBI hybrids **7a**, **7d** and **10a** against CDK2/Cyclin A2.

Compound	IC_{50} (nM) CDK2
7a	96.46 ± 5.3
7d	26.24 ± 1.4
10a	42.95 ± 2.3
Staurosporine	38.5 ± 2.1

GIT absorption as they were located in the white area of Human Intestinal absorption in Boiled egg chart [60] (Fig. 6). These three compounds, **7a**, **7d**, and **10a**, might have no penetration ability to the BBB as they were located away from the yellow area of BBB penetrations and thus, they could be used safely for peripheral tumors with no CNS complication.

The high bioavailability of the three leads could be attributed to their optimum physicochemical properties as demonstrated by the bioavailability radar chart (Fig. 7). The chart contains six critical parameters for oral absorption: FLEX (Flexibility), LIPO (Lipophilicity), INSATU (Saturation), INSOLU (Solubility), SIZE and POLAR (Polarity). The chart

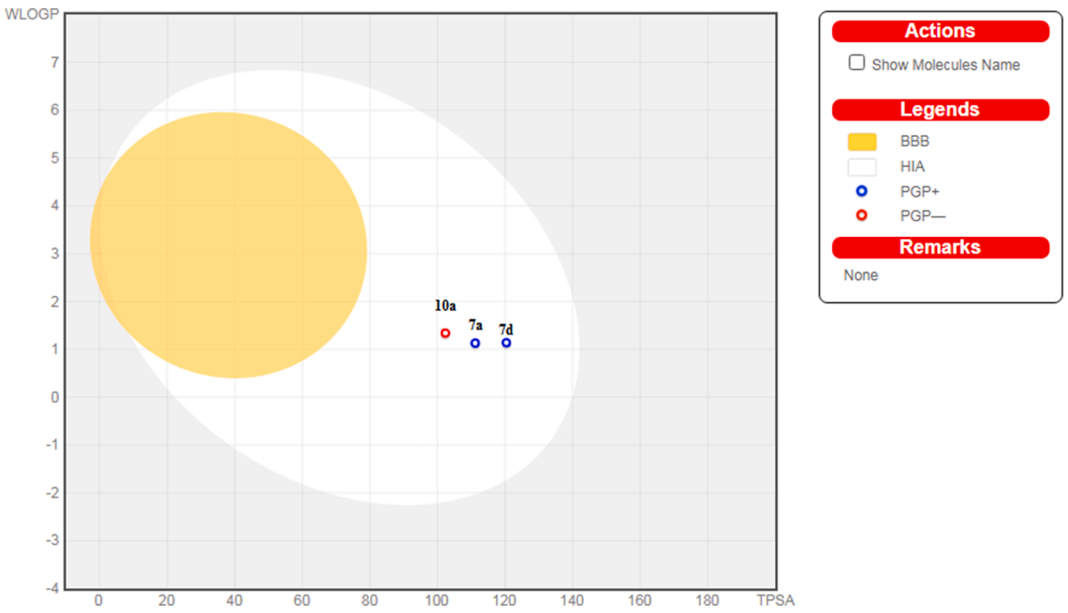

Fig. 6. Boiled Egg chart showing the oral absorption of the synthesized hybrids (**7a**, **7d** and **10a**) and their ability to penetrate the BBB.

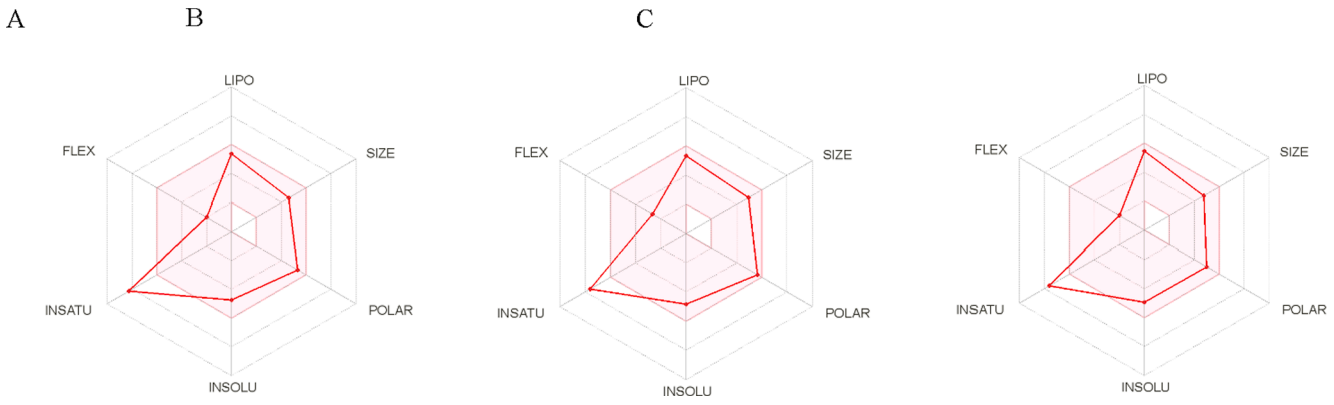

Fig. 7. The oral bioavailability radar chart of the tested hybrids. (A) **7a** (B) **7d** (C) **10a**. The pink area represents the range of the optimal property values for oral bioavailability and the red lines are the predicted properties. (For interpretation of the references to color in this figure legend, the reader is referred to the web version of this article.)

Table 3
The *in silico* predicted ADME and medicinal chemistry properties of the most active hybrids**7a**, **7d** and **10a**.

Parameter	7a	7d	10a
GIA	High	High	High
BBB	No	No	No
P-gP substrate	Yes	Yes	Yes
CYP1A2 inhibitor	Yes	Yes	Yes
CYP2C19 inhibitor	Yes	Yes	Yes
CYP2C9 inhibitor	Yes	Yes	Yes
CYP2D6 inhibitor	Yes	Yes	Yes
CYP3A4 inhibitor	Yes	Yes	Yes
Veber Violations	0	0	0
LipinskiViolations	0	0	0

GIA (gastrointestinal absorption), BBB (Blood Brain Barrier), PgP (P-glyco protein transporter), CYP1A2, CYP2C19, CYP2C9, CYP2D6 and CYP3A4 are the five major isoforms of cytochromes P450 (CYP). PAINS (Pan Assay Interference Structures). Veber's rule summarized as number of rotatable bonds $\leq$ 10 and the TPSA $\leq$ 140 A. Lipinski rule summarized as MWT $\leq$ 500, Number of hydrogen bond acceptors $\leq$ 10, Number of hydrogen bond donors $\leq$ 5 and LogP $\leq$ 5.

contains a pink area representing the optimal range of the six properties and red lines representing the predicted physicochemical properties of the compounds (Fig. 7). All the physicochemical properties of hybrids (**7a**, **7d** and **10a**) were located in the desired range of all parameters except for the INSATU (saturation) (Fig. 7).

The metabolism of the three examined hybrids, as most of drugs, are predicted to take part in the liver by the CYTP450 enzymes, so they are suggested to be administered alone to minimize the possible drug-drug interactions. On the other hand, these hybrids were found to have no violations in all drug likeness rules (Lipinski, Veber and Muegge) with only alertness for PAINS assay due to the presence of exocyclic imine functionality [61,62]. Table 3 summarizes all the predicted ADME and medicinal chemistry properties of the three lead hybrids. In conclusion, it was found that isatin-TBI hybrids (**7a**, **7d** and **10a**) demonstrated not only good biological actions but also an acceptable predicted ADME and physicochemical properties.

2.3.2. *Docking results*

One of the most valuable drug design techniques is the docking strategy which has been implemented in many research works to provide insights about the possible binding modes of drugs to their targets, as well as predicting their affinities by scoring them according to energy

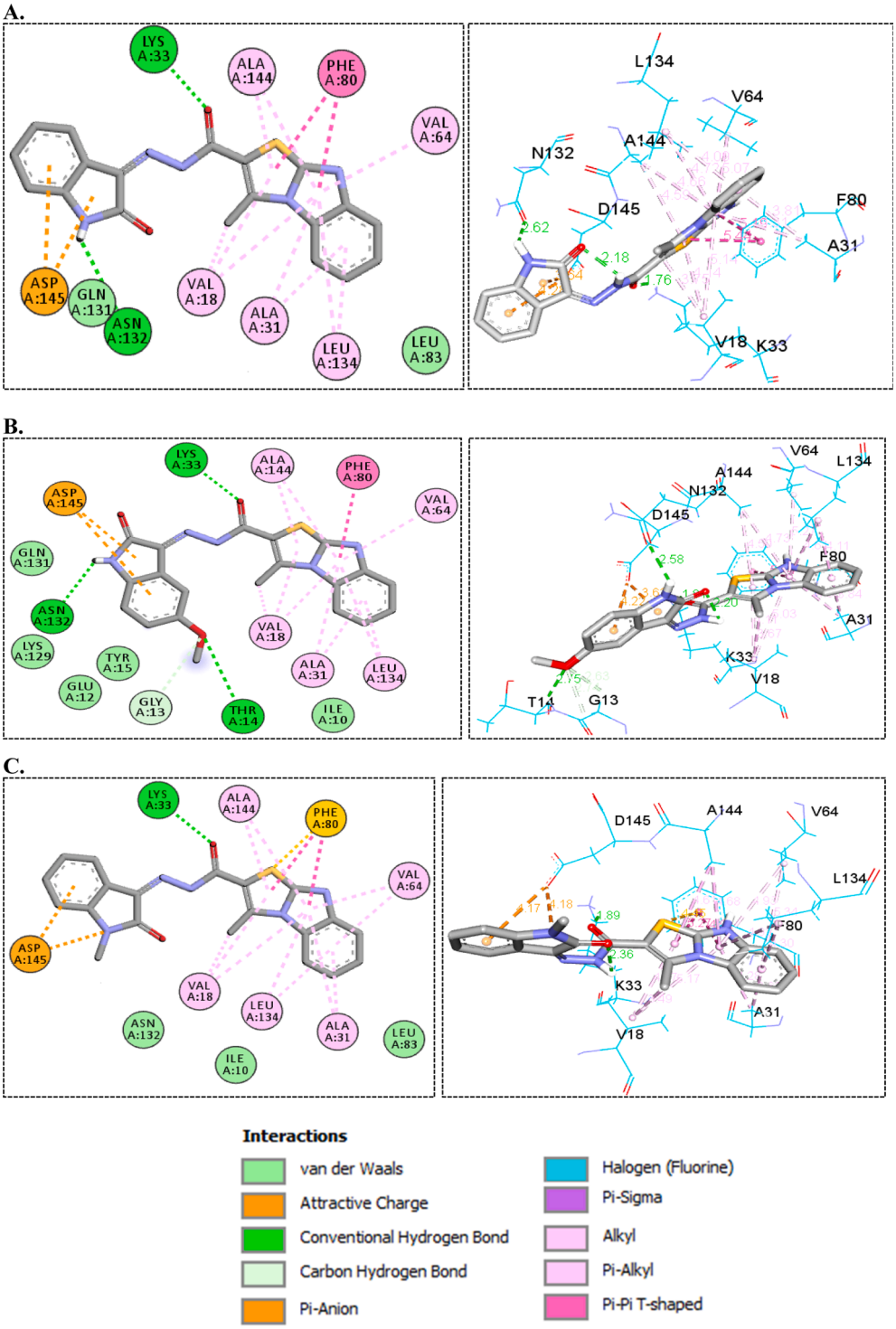

Fig. 8. 2D (Left side) and 3D (right side) interactions of the three Leads (A) **7a** (B) **7d** (C) **10a**.

and interactions. But docking is an error prone technique and should always be validated either by comparison to experimental reference or further supported by molecular dynamics results.

In this regard, the co-crystalized ligand was re-docked to its CDK2 enzyme. The calculated RMSD values between the co-crystalized ligand and docked pose were 0.62 Å in the presence of water and 0.7 Å in the absence of water, so the water molecules were removed to increase the diversity of selected compounds [63]. All the explored isatin-TBI hybrids (**7a**, **7d** and **10a**) achieved high binding affinities and strong interaction patterns with their target even more than the reference ligand which achieved a score of −9.5 Kcal/mole. Hybrid **7d** achieved the highest score with −11.2 Kcal/mole, whereas, hybrids **7a** and **10a** achieved scores of −10.4 and −10.9 Kcal/mole, respectively. Interestingly, the three hybrids were able to form diverse types of interaction, with large number of bonds.

The outcomes of the docking simulations for isatin-TBI hybrids (**7a**,

Table 4
The detailed interaction and binding scores of the lead compounds **7a**, **7d** and **10a**.

Compound	Score (Kcal \Mole)	Bond type	Distance
7a	−10.4	Hydrogen bond with LYS33	1.71
		Hydrogen bond with ASN132	2.62
		Pi-Anion interaction with ASP145	4.28
		Pi-Anion interaction with ASP145	3.64
		Pi-Pi with PHE80	5.44
		Pi-Pi with PHE80	5.19
		Alkyl-Alkyl with VAL18	3.75
		Pi-Alkyl with VAL18	4.14
		Pi-Alkyl with VAL18	5.14
		Pi-Alkyl with LEU134	4.09
		Pi-Alkyl with LEU134	4.72
		Pi-Alkyl with ALA144	4.66
		Pi-Alkyl with ALA144	4.59
		Pi-Alkyl with ALA31	3.81
		Pi-Alkyl with ALA31	4.31
		Pi-Alkyl with VAL64	5.07
7d	−11.2	Hydrogen bond with LYS33	1.81
		Hydrogen bond with ASN132	2.58
		Hydrogen bond with THR14	2.75
		Pi-Anion interaction with ASP145	3.62
		Pi-Anion interaction with ASP145	4.22
		Non-classical carbon Hydrogen bond with GLY13	2.63
		Non-classical carbon Hydrogen bond with GLY13	2.74
		Pi-Pi with PHE80	5.44
		Alkyl-Alkyl with VAL18	3.67
		Pi-Alkyl with VAL18	5.03
		Pi-Alkyl with VAL18	4.11
		Pi-Alkyl with LEU134	4.11
		Pi-Alkyl with LEU134	4.61
		Pi-Alkyl with ALA144	4.59
		Pi-Alkyl with ALA144	4.73
		Pi-Alkyl with ALA144	2.83
		Pi-Alkyl with ALA31	4.30
		Pi-Alkyl with ALA31	3.84
		Pi-Alkyl with VAL64	5.27
10a	−10.9	Hydrogen bond with LYS33	3.62
		Ionic interaction with ASP145	1.89
		Pi-Anion interaction with ASP145	4.18
		Pi-Pi with PHE80	4.17
		Pi-Pi with PHE80	5.27
		Pi-Sulfur with PHE80	4.92
		Alkyl-Alkyl with VAL18	4.45
		Pi-Alkyl with VAL18	3.49
		Pi-Alkyl with VAL18	5.17
		Pi-Alkyl with LEU134	4.17
		Pi-Alkyl with LEU134	4.30
		Pi-Alkyl with ALA144	4.92
		Pi-Alkyl with ALA144	4.68
		Pi-Alkyl with ALA31	4.61
		Pi-Alkyl with ALA31	4.28
		Pi-Alkyl with VAL64	4.96
		Pi-Alkyl with VAL64	5.34

7d and **10a**) unveiled, as expected, the ability of the tricyclic thiazolo [3,2-*a*]benzimidazole ring to well-accommodate in a hydrophobic pocket within the CDK2 binding site, establishing several hydrophobic interactions with non-polar residues lining this pocket, such as VAL18, ALA31, VAL64, PHE80, LEU134 and ALA144.

On the other hand, inspection of the docking poses for the examined hybrids revealed the ability of oxindole ring in both *N*-unsubstituted hybrids **7a** and **7d** to be engaged in a hydrogen bond interaction *via* its (NH) functionality with ASN132 amino acid residue. Moreover, the docking simulations for hybrids **7a**, **7d** and **10a** revealed a binding interaction in which the (C═O) of the hydrazide spacer acted as an essential H-bond acceptor for LYS33 in the CDK2 binding site (Fig. 8).

Worthy of note, substitution of oxindole moiety with 5-methoxy group in hybrid **7d** resulted in an extra hydrogen bond interaction with THR14 which may explain its superior *in vitro* CDK2 inhibitory activity (IC_{50} = 26.24 nM) over hybrids **7a** and **10a** (IC_{50} = 42.95 and 96.46 nM, respectively, Table 2). Regrettably, the TBI sp2 nitrogen didn't engage a hydrogen bond within the CDK2 active site. The detailed interactions established by the three examined hybrids **7a**, **7d** and **10a** within the CDK2 active site were summarized in Table 4.

2.3.3. Molecular dynamics

In the past few decades, molecular dynamics (MD) has been implemented as an inevitable tool for drug discovery studies. It has proven its worth in identification of potential inhibitors for promising targets, studying the nature of macromolecules or interpretations of drug resistances [64–66]. In this work, MD has been conducted to validate the predicted binding mode from the docking study. As docking provides only a preferred static conformation, it is more reliable to monitor the binding strength between a ligand and its target enzyme for a period of times (usually in Nano seconds) using MD simulations. RMSD provided from MD simulations is a trusted parameter to judge the stability of a ligand-target complex. RMSD reached at the maximum dynamicity 1.24 Å for hybrid **7d**, while reached 1.67 Å and 1.58 Å for hybrids **7a** and **10a**, respectively (Fig. 9)**.** This indicates the greater ability of hybrid **7d** to form a stable complex with CDK2 enzyme than hybrids **7a** and **10a**.

This ability is assumed to be due to the extra hydrogen bonding with THR14 achieved by the additional 5-methoxy group of hybrid **7d**, thus this assumption was validated by measuring the stability of the formed hydrogen bonds between each ligand and the CDK2 enzyme through the entire MD simulation using GROMACS built-in commands for measuring hydrogen bond distances. Generally, the distance between the hydrogen bond donor and the hydrogen bond acceptor in a valid hydrogen bond should be always less than 3.5 Å. This condition was maintained in all the formed hydrogen bonds for the three hybrids which indicates a stable valid binding (Table 5).

2.3.4. MM-PBSA binding free energy calculations

Another valuable indicator to assess the strength of binding between a ligand and its target is the calculated MM-PBSA binding free energy generated by MD simulations. This is more reliable than the single conformation-based score calculated from than docking study, as in MD simulation, the binding free energies are calculated for every conformation saved in the trajectory. Thus, the g_mmpbsa package was implemented to calculate the MM-PBSA binding free energy for the three complexes by using MmPbSaStat.py python script which allows the package to calculate the total free energy for each component of the complex i.e. (the energy of the complex, receptor and the ligand, etc.). Furthermore, the free energy for each component could be calculated by the cumulative sum of its molecular mechanics potential energy in a vacuum and the free energy of solvation. The free energy of solvation includes the polar solvation energy (electrostatic) and nonpolar solvation energy (non-electrostatic) [67]. One of the most widely used nonpolar models is the solvent accessible surface area (SASA) [67]. All those types of energies were calculated by the g_mmpbsa package along with the values standard deviation and then summed together to yield the average total free energy of each component. Finally, the binding free energy could be calculated by subtracting the total free energy of the receptor and the total free energy of the ligand from the total free energy of the complex. The binding free energy of isatin-TBI hybrids **7a**, **7d** and **10a** are summarized in Table 6. Complexes with lesser binding free energy are considered to be more stable and have stronger binding interactions.

Generally, **7d**–CDK2 complex was better than **7a** and **10a** complexes in the binding free energy. Its average binding free energy reached −323.69 ± 15.17, while **7a** and **10a** average binding free energy reached −298.47 ± 15.17 and −311.49 ± 15.37 kJ/mol, respectively. The overall results of the three dynamic simulations supported and validated the proposed binding mode for the examined hybrids, as well as ascribed to hybrid **7d** a higher affinity and stronger binding

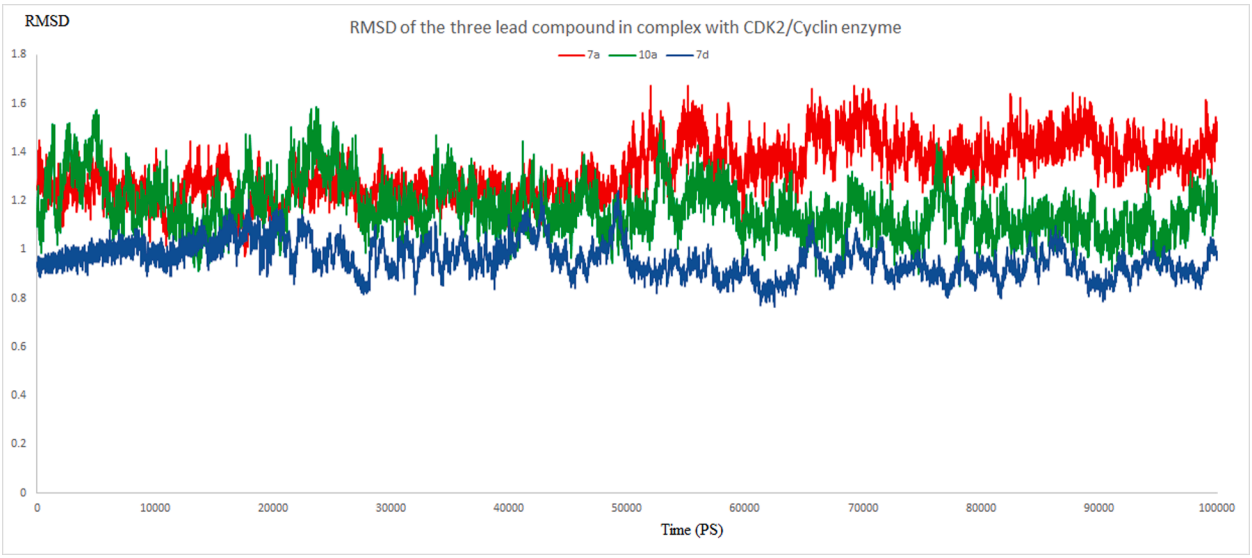

Fig. 9. RMSD of 100 ns MD simulations for isatin-TBI hybrids (**7a**, **7d** and **10a**) in complex with CDK2.

Table 5
The average distances of all the hydrogen bonds formed between hybrids **7a**, **7d** and **10a** and CDK2 through the entire 100 ns MD simulation.

Compound	Hydrogen bond name	Average distance (A^0) ± SD
7a	Hydrogen bond with LYS33	1.75 ± 0.11
	Hydrogen bond with ASN132	2.57 ± 0.1
7d	Hydrogen bond with LYS33	1.90 ± 0.13
	Hydrogen bond with ASN132	2.64 ± 0.07
	Hydrogen bond with	2.73 ± 0.05
10a	Hydrogen bond with LYS33	1.83 ± 0.09

Table 6
MM-PBSA calculations of the binding free energy for the three complexes; **7a**, **7d** and **10a**.

Complex	$\Delta E_{binding}$ (kj/mol)	$\Delta E_{Electrostatic}$ (kj/mol)	$\Delta E_{Vander\ Waal}$ (kj/mol)	ΔE_{polar} solvation (kj/mol)	SASA (kj/mol)
7a	−298.47 ± 11.52	−107.22 ± 14.36	−268.13 ± 16.45	100.40 ± 12.03	−23.52 ± 1.74
7d	−323.69 ± 15.17	−120.36 ± 14.51	−277.85 ± 17.06	102.14 ± 11.95	−27.62 ± 2.01
10a	−311.49 ± 15.37	−117.20 ± 15.13	−270.34 ± 16.98	103.22 ± 12.18	−27.17 ± 1.84

interaction, which could be attributed to incorporation of the methoxy group that was involved in an extra hydrogen bonding with CDK2 active site.

3. Conclusions

In the present study, replacement of indole moiety in the previously reported oxindole-based compounds with a thiazolo[3,2-*a*]benzimidazole one, resulted in development of promising CDK2 inhibitors that showed excellent anti-proliferative activity towards breast cancer cell lines. All the synthesized hybrids (**7a–e** and **10a–i**) were characterized for their potential anti-proliferative action towards MDA-MB-231 and MCF-7 breast cancer cell lines. The *N*-unsubstituted oxindole series **7a–e** showed moderate to excellent cytotoxic activity with IC_{50} ranged from 2.02 ± 0.13 μM to 42.64 ± 2.9 μM against both cell lines. **7a** was the most active derivative against MCF-7 cell line with IC_{50} = 2.02 ± 0.13 μM, whereas **7d** was the most active hybrid against MDA-MB-231 cell line with IC_{50} = 3.30 ± 0.21 μM, and both showed superior activity to the reference drug Staurosporine. Similarly, the *N*-substituted series **10a–i** revealed moderate to excellent activity and the most active derivative **10a** had IC_{50} = 2.60 ± 1.47 μM and 3.01 ± 0.22 μM towards MDA-MB-231 and MCF-7cell line, respectively. In addition, cell cycle analysis for the most active compounds **7a**, **7d** and **10a** showed remarkable decrease in the cell population at the G0/G1 phase with concomitant elevation of G2/M phase suggested that the cell cycle was mainly arrested in the G2/M phase in both cell lines. Furthermore, an Annexin V-FITC/PI analysis evidenced that the three candidates were able to induce an approximately (11.9-, 19.9- and 24.8-fold) and (32.0-, 16.6- and 25.0-fold) total apoptosis increase in MDA-MB-231 and MCF-7cell lines, respectively, compared to the control. The results of CDK2 inhibitory activity for hybrids **7a**, **7d** and **10a**, showed that **7d** was the most potent one with IC_{50} value of 26.24 nM that was superior to the reference drug, Staurosporine which exhibited IC_{50} value of 38.5 nM, followed by compounds **10a** and **7a**. These results gave indications that the anti-proliferative activity might be due to inhibition of CDK2 enzyme. The docking simulations unveiled, as expected, the ability of the TBI ring to well-accommodate and establish several hydrophobic interactions within a hydrophobic pocket in the CDK2 binding site. Also, the docking simulations highlighted the significance of incorporation of the hydrazide linker and isatin unsubstituted (NH) functionality in the H-bonding interactions. Interestingly, the most potent CDK2 inhibitor **7d** achieved the best binding score (-11.2 Kcal/mole) and formed the most stable complex with CDK2 enzyme (RMSD = 1.24 Å) in a 100 ns MD simulation. In addition, the MM-PBSA calculations ascribed the lowest binding free energy to the **7d**–CDK2 complex (−323.69 ± 15.17 kJ/mol). This could be attributed to an incorporation of the 5-OCH_3 group that was engaged in an extra hydrogen bonding with key THR14 amino acid. Collectively, these results suggested compound **7d** as a good candidate for further optimization as promising breast cancer antitumor agent and CDK2 inhibitor.

4. Experimental

4.1. Chemistry

4.1.1. General

The NMR spectra have been recorded by Bruker spectrometer at 400 MHz. ^{13}C NMR spectra were run at 100 MHz in deuterated dimethylsulfoxide (DMSO-*d6*). Chemical shifts (δ_H) are reported relative to the solvent (DMSO-d_6). Infrared spectra were recorded on Schimadzu FT-IR 8400S spectrophotometer. Elemental analyses were performed

using FLASH 2000 CHNS/O analyzer, Thermo Scientific at the Regional Center for Mycology and Biotechnology (RCMB), Al-Azhar University, Cairo. All reagents and solvents were purified and dried by standard techniques. The purity of the prepared hybrids was greater than 95%, as determined by HPLC analysis. Intermediates **4** [68,69] and **9a-i** were prepared as described previously [48,70].

*4.1.2. Synthesis of 3-methylbenzo[4,5]imidazo[2,1-b]thiazole-2-carbohydrazide **5***

To a stirred hot solution of ethyl 3-methylbenzo[4,5]imidazo[2,1-*b*]thiazole-2-carboxylate **4** (1 g, 3.8 mmol) in 30 mL of isopropyl alcohol, hydrazine hydrate (0.25 mL, 7.5 mmol) was added. The reaction mixture was refluxed for 6 h, and then poured onto ice water. The formed precipitate was collected under vacuum, washed with diethyl ether and recrystallized from DMF/EtOH mixture to furnish the key intermediate **5** in a good yield (88%) [68].

*4.1.3. Synthesis of targeted final compounds **7a-e** and **10a-i***

3-Methylbenzo[4,5]imidazo[2,1-*b*]thiazole-2-carbohydrazide **5** (0.3 g, 1.2 mmol) was heated with equivalent amount of different isatin derivatives (**6a-e** or **9a-i**) in glacial acetic acid for 3–5 h with TLC monitoring. On completion of the reaction, the contents of flask cooled to room temperature, the formed product was collected by filtration, washed with water and petroleum ether and recrystallized form dioxane/EtOH mixture to furnish the final compounds **7a-e** and **10a-i**, respectively.

*4.1.3.1. 3-Methyl-N'-(2-oxoindolin-3-ylidene)benzo[4,5]imidazo[2,1-b]thiazole-2-carbohydrazide **7a**.* Yellow powder (yield 82%), m.p. >300 °C; ^{1}H NMR δ *ppm*: 3.23 (s, 3H, CH_3), 6.97 (d, 1H, Ar—H, J = 8.0 Hz), 7.14 (t, 1H, Ar—H, J = 8.0 Hz), 7.32 (t, 1H, Ar—H, J = 8.0 Hz), 7.40–7.46 (m, 2H, Ar—H), 7.67 (d, 1H, Ar—H, J = 8.0 Hz), 7.73 (d, 1H, Ar—H, J = 8.0 Hz), 8.10 (d, 1H, Ar—H, J = 8.0 Hz), 11.35 (s, 1H, NH of 2-indolinone), 12.99 (s, 1H, NH of hydrazide spacer); ^{13}C NMR δ *ppm*: 14.81 (CH_3), 111.81, 113.46, 117.68, 119.20, 119.98, 121.84, 123.35, 124.92, 127.54, 128.84, 132.53, 135.09, 138.05, 138.97, 143.16, 148.84, 163.09 (C═O 2-indolinone), 168.96 (C═O hydrazide spacer); IR (KBr, ν cm^{-1}) 3280, 3245 (2NH) and 1723, 1705 (2C═O); MS *m/z* [%]: 375 [M$^+$, 6.47], 90 [100]; Anal. Calcd. for $C_{19}H_{13}N_5O_2S$: C, 60.79; H, 3.49; N, 18.66; found C, 60.95; H, 3.46; N, 18.58; HPLC (t_{ret}) = 4.37 min (98.1% at 254 nm).

*4.1.3.2. N'-(5-Fluoro-2-oxoindolin-3-ylidene)-3-methylbenzo[4,5]imidazo[2,1-b]thiazole-2-carbohydrazide **7b**.* Red powder (yield 75%), m.p. >300 °C; ^{1}H NMR δ *ppm*: 3.20 (s, 3H, CH_3), 6.94–6.97 (m, 1H, Ar—H), 7.20 (t, 1H, Ar—H, J = 9.0 Hz), 7.29 (t, 1H, Ar—H, J = 8.0 Hz), 7.39–7.45 (m, 2H, Ar—H), 7.70 (d, 1H, Ar—H, J = 8.0 Hz), 8.08 (d, 1H, Ar—H, J = 8.0 Hz), 11.23 (s, 1H, NH of 2-indolinone), 13.03 (s, 1H, NH of hydrazide spacer); ^{13}C NMR δ *ppm*: 21.50 (CH_3), 112.89, 113.44, 119.19, 120.81, 121.83, 122.62, 123.64, 124.91, 130.46, 134.08, 139.40, 142.32, 149.52, 152.30, 155.69, 157.67, 160.74 (C═O 2-indolinone), 172.54 (C═O hydrazide spacer); IR (KBr, ν cm^{-1}) 3300, 3240 (2NH) and 1735, 1702 (2C═O); MS *m/z* [%]: 393 [M$^+$, 16.30], 142 [100]; Anal. Calcd. for $C_{19}H_{12}FN_5O_2S$: C, 58.01; H, 3.07; N, 17.80; found C, 57.78; H, 3.12; N, 17.93; HPLC (t_{ret}) = 3.90 min (97.3% at 254 nm).

*4.1.3.3. N'-(5-Bromo-2-oxoindolin-3-ylidene)-3-methylbenzo[4,5]imidazo[2,1-b]thiazole-2-carbohydrazide **7c**.* Orange powder (yield 79%), m.p. >300 °C; ^{1}H NMR δ *ppm*: 3.22 (s, 3H, CH_3), 6.88 (d, 1H, Ar—H, J = 8.5 Hz), 7.28 (t, 1H, Ar—H, J = 8.5 Hz), 7.38 (t, 1H, Ar—H, J = 8.0 Hz), 7.52 (d, 1H, Ar—H, J = 8.0 Hz), 7.68–7.70 (m, 2H, Ar—H), 8.06 (d, 1H, Ar—H, J = 8.0 Hz), 11.32 (s, 1H, NH of 2-indolinone), 13.01 (s, 1H, NH of hydrazide spacer); IR (KBr, ν cm^{-1}) 3295, 3271 (2NH) and 1732, 1701 (2C═O); Anal. Calcd. for $C_{19}H_{12}BrN_5O_2S$: C, 50.23; H, 2.66; N, 15.42; found C, 50.41; H, 2.64; N, 15.33; HPLC (t_{ret}) = 5.21 min (97.9% at 254 nm).

*4.1.3.4. N'-(5-Methoxy-2-oxoindolin-3-ylidene)-3-methylbenzo[4,5]imidazo[2,1-b]thiazole-2-carbohydrazide **7d**.* Red powder (yield 84%), m.p. >300 °C; ^{1}H NMR δ *ppm*: 3.22 (s, 3H, CH_3), 3.79 (s, 3H, OCH_3), 6.85 (d, 1H, Ar—H, J = 9.0 Hz), 6.95 (d, 1H, Ar—H, J = 8.0 Hz), 7.14 (s, 1H, Ar—H), 7.28 (t, 1H, Ar—H, J = 8.0 Hz), 7.38 (t, 1H, Ar—H, J = 7.5 Hz), 7.69 (d, 1H, Ar—H, J = 8.5 Hz), 8.06 (d, 1H, Ar—H, J = 8.5 Hz), 11.02 (s, 1H, NH of 2-indolinone), 13.10 (s, 1H, NH of hydrazide spacer); IR (KBr, ν cm^{-1}) 3320, 3341 (2NH) and 1721, 1700 (2C═O); MS *m/z* [%]: 405 [M$^+$, 91.54], 102 [100]; Anal. Calcd. for $C_{20}H_{15}N_5O_3S$: C, 59.25; H, 3.73; N, 17.27; found C, 58.92; H, 3.78; N, 17.34; HPLC (t_{ret}) = 4.85 min (96.4% at 254 nm).

*4.1.3.5. N'-(5-Nitro-2-oxoindolin-3-ylidene)-3-methylbenzo[4,5]imidazo[2,1-b]thiazole-2-carbohydrazide **7e**.* Yellow powder (yield 72%), m.p. >300 °C; ^{1}H NMR δ *ppm*: 3.23 (s, 3H, CH_3), 7.07 (d, 1H, Ar—H, J = 8.5 Hz), 7.29–7.34 (m, 1H, Ar—H), 7.39 (t, 1H, Ar—H, J = 8.5 Hz), 7.71 (t, 1H, Ar—H, J = 7.5 Hz), 8.08 (t, 1H, Ar—H, J = 7.5 Hz), 8.28–8.32 (m, 2H, Ar—H), 11.85 (s, 1H, NH of 2-indolinone), 12.87 (s, 1H, NH of hydrazide spacer); IR (KBr, ν cm^{-1}) 3324, 3301 (2NH) and 1718, 1710 (2C═O); Anal. Calcd. for $C_{19}H_{12}N_6O_4S$: C, 54.28; H, 2.88; N, 19.99; found C, 54.03; H, 2.91; N, 20.11; HPLC (t_{ret}) = 6.09 min (98.5% at 254 nm).

*4.1.3.6. 3-Methyl-N'-(1-methyl-2-oxoindolin-3-ylidene)benzo[4,5]imidazo[2,1-b]thiazole-2-carbohydrazide **10a**.* Yellow powder (yield 80%), m.p. >300 °C; ^{1}H NMR δ *ppm*: 1.92 (s, 3H, *N*-CH_3), 3.22 (s, 3H, CH_3), 7.17 (d, 1H, Ar—H, J = 8.0 Hz), 7.23 (d, 1H, Ar—H, J = 8.0 Hz), 7.32 (t, 1H, Ar—H, J = 8.0 Hz), 7.42 (t, 1H, Ar—H, J = 8.0 Hz), 7.49 (t, 1H, Ar—H, J = 8.0 Hz), 7.70–7.75 (m, 2H, Ar—H), 8.10 (d, 1H, Ar—H, J = 8.0 Hz), 13.01 (s, 1H, NH of hydrazide spacer); ^{13}C NMR δ *ppm*: 21.50 (CH_3), 28.11 (*N*-CH_3), 110.33, 112.77, 115.57, 119.84, 125.35, 127.89, 131.09, 136.41, 138.37, 140.09, 142.64, 144.68, 146.94, 148.02, 153.60, 155.83, 159.86 (C═O 2-indolinone), 172.60 (C═O hydrazide spacer); IR (KBr, ν cm^{-1}) 3345 (NH) and 1720, 1695 (2C═O); MS *m/z* [%]: 389 [M$^+$, 100]; Anal. Calcd. for $C_{20}H_{15}N_5O_2S$: C, 61.68; H, 3.88; N, 17.98; found C, 61.82; H, 3.85; N, 18.07; HPLC (t_{ret}) = 5.72 min (97.8% at 254 nm).

*4.1.3.7. 3-Methyl-N'-(2-oxo-1-propylindolin-3-ylidene)benzo[4,5]imidazo[2,1-b]thiazole-2-carbohydrazide **10b**.* Yellow powder (yield 68%), m.p. 267–269 °C; ^{1}H NMR δ *ppm*: 0.90 (t, 3H, —CH_2—$\underline{CH_3}$, J = 7.5 Hz), 1.67–1.69 (m, 2H, —$\underline{CH_2}$—CH_3), 3.21 (s, 3H, CH_3), 3.71(t, 2H, *N*-CH_2, J = 7.0 Hz), 7.18–7.22 (m, 2H, Ar—H), 7.29 (t, 1H, Ar—H, J = 7.5 Hz), 7.39 (t, 1H, Ar—H, J = 7.5 Hz), 7.45 (t, 1H, Ar—H, J = 8.5 Hz), 7.69–7.71 (m, 2H, Ar—H), 8.07 (d, 1H, Ar—H, J = 8.0 Hz), 12.95 (s, 1H, NH of hydrazide spacer); ^{13}C NMR δ *ppm*: 10.93 (—CH2—CH3), 14.13 (—CH3), 20.18 (—CH2—CH3), 40.75 (*N*-CH2), 110.10, 112.74, 118.57, 118.79, 119.84, 120.96, 121.11, 122.07, 123.08, 124.18, 125.74, 129.92, 131.72, 131.24, 143.15, 148.33, 160.62 (C═O 2-indolinone), 169.75 (C═O hydrazide spacer); IR (KBr, ν cm^{-1}) 3304 (NH) and 1715, 1701 (2C═O); Anal. Calcd. for $C_{22}H_{19}N_5O_2S$: C, 63.29; H, 4.59; N, 16.78; found C, 62.96; H, 4.64; N, 16.75; HPLC (t_{ret}) = 6.24 min (99.0% at 254 nm).

*4.1.3.8. N'-(1-Allyl-2-oxoindolin-3-ylidene)-3-methylbenzo[4,5]imidazo[2,1-b]thiazole-2-carbohydrazide **10c**.* Orange powder (yield 71%), m.p. 283–285 °C; ^{1}H NMR δ *ppm*: 3.22 (s, 3H, CH_3), 4.41 (br s, 2H, *N*—CH_2), 5.19–5.27 (m, 2H, =CH_2), 5.86–5.91 (m, 1H, *N*—CH_2—$\underline{CH}$), 7.11 (d, 1H, Ar—H, J = 8.5 Hz), 7.19 (t, 1H, Ar—H, J = 7.5 Hz), 7.30 (t, 1H, Ar—H, J = 7.5 Hz), 7.40–7.48 (m, 2H, Ar—H), 7.72 (d, 2H, Ar—H, J = 7.5 Hz), 8.10 (d, 1H, Ar—H, J = 8.0 Hz), 13.01 (s, 1H, NH of hydrazide spacer); IR (KBr, ν cm^{-1}) 3312 (NH) and 1720, 1711 (2C═O); MS *m/z* [%]: 415 [M$^+$, 36.30], 414 [100]; Anal. Calcd. for $C_{22}H_{17}N_5O_2S$: C,

63.60; H, 4.12; N, 16.86; found C, 63.77; H, 4.17; N, 16.79; HPLC (t_{ret}) = 3.83 min (96.7% at 254 nm).

4.1.3.9. N'-(1-Benzyl-2-oxoindolin-3-ylidene)-3-methylbenzo[4,5]imidazo[2,1-b]thiazole-2-carbohydrazide ***10d.*** Yellow powder (yield 77%), m.p. >300 °C; ^{1}H NMR δ *ppm*: 3.23 (s, 3H, CH_3), 5.00 (s, 2H, *N*—CH_2), 7.03 (d, 1H, Ar—H, *J* = 8.0 Hz), 7.13–7.22 (m, 2H, Ar—H), 7.28 (d, 1H, Ar—H, *J* = 8.0 Hz), 7.32–7.36 (m, 2H, Ar—H), 7.38–7.46 (m, 4H, Ar—H), 7.72 (d, 2H, Ar—H, *J* = 8.0 Hz), 8.09–8.12 (m, 1H, Ar—H), 12.98 (s, 1H, NH of hydrazide spacer); ^{13}C NMR δ *ppm*: 21.47 (CH_3), 46.45(*N*—CH_2), 110.81, 113.47, 116.37, 117.57, 121.58, 123.85, 124.67, 128.74, 133.86, 135.12, 136.84, 137.22, 140.15, 142.20, 144.16, 145.52, 145.72, 151.78, 153.59, 158.48, 159.16, 161.87 (C═O 2-indolinone), 172.74 (C═O hydrazide spacer); IR (KBr, ν cm^{-1}) 3324 (NH) and 1745, 1715, 1698 (3C═O); MS *m/z* [%]: 465 [M^+, 27.45], 91 [100]; Anal. Calcd. for $C_{26}H_{19}N_5O_2S$: C, 67.08; H, 4.11; N, 15.04; found C, 66.89; H, 4.14; N, 15.11; HPLC (t_{ret}) = 4.17 min (98.5% at 254 nm).

4.1.3.10. N'-(1-(3-Fluorobenzyl)-2-oxoindolin-3-ylidene)-3-methylbenzo[4,5]imidazo[2,1-b]thiazole-2-carbohydrazide ***10e.*** Red powder (yield 82%), m.p. 289–290 °C; ^{1}H NMR δ *ppm*: 3.22 (s, 3H, CH_3), 5.01 (s, 2H, *N*—CH_2), 7.04 (d, 1H, Ar—H, *J* = 8.0 Hz), 7.09 (t, 1H, Ar—H, *J* = 8.0 Hz), 7.19 (t, 1H, Ar—H, *J* = 7.5 Hz), 7.23 (t, 1H, Ar—H, *J* = 7.5 Hz), 7.31 (t, 1H, Ar—H, *J* = 8.0 Hz), 7.37–7.42 (m, 4H, Ar—H), 7.72 (t, 2H, Ar—H, *J* = 8.5 Hz), 8.10 (d, 1H, Ar—H, *J* = 8.0 Hz), 12.92 (s, 1H, NH of hydrazide spacer); IR (KBr, ν cm^{-1}) 3309 (NH) and 1712, 1701 (2C═O); Anal. Calcd. for $C_{26}H_{18}FN_5O_2S$: C, 64.59; H, 3.75; N, 14.48; found C, 64.72; H, 3.76; N, 14.55; HPLC (t_{ret}) = 5.06 min (98.2% at 254 nm).

4.1.3.11. N'-(1-(4-Fluorobenzyl)-2-oxoindolin-3-ylidene)-3-methylbenzo[4,5]imidazo[2,1-b]thiazole-2-carbohydrazide ***10f.*** Red powder (yield 73%), m.p. >300 °C; ^{1}H NMR δ *ppm*: 3.23 (s, 3H, CH_3), 4.99 (s, 2H, *N*—CH_2), 7.06 (d, 1H, Ar—H, *J* = 7.5 Hz), 7.13–7.21 (m, 3H, Ar—H), 7.30 (t, 1H, Ar—H, *J* = 8.0 Hz), 7.39–7.47 (m, 4H, Ar—H), 7.71–7.74 (m, 2H, Ar—H), 8.09 (d, 1H, Ar—H, *J* = 8.0 Hz), 12.91 (s, 1H, NH of hydrazide spacer); ^{13}C NMR δ *ppm*: 14.83 (CH_3), 42.39 (*N*-CH_2), 111.02, 113.48, 115.88, 116.09, 119.20, 119.57, 121.86, 122.55, 124.04, 124.93, 126.56, 128.76, 130.06, 130.14, 132.32, 135.31, 138.61, 143.24, 145.54, 148.84, 154.29, 156.73, 160.29 (C═O 2-indolinone), 169.17 (C═O hydrazide spacer); IR (KBr, ν cm^{-1}) 3356 (NH) and 1721, 1703 (2C═O); Anal. Calcd. for $C_{26}H_{18}FN_5O_2S$: C, 64.59; H, 3.75; N, 14.48; found C, 64.81; H, 3.72; N, 14.53; HPLC (t_{ret}) = 5.18 min (96.2% at 254 nm).

4.1.3.12. N'-(1-(4-Cyanobenzyl)-2-oxoindolin-3-ylidene)-3-methylbenzo[4,5]imidazo[2,1-b]thiazole-2-carbohydrazide ***10g.*** Yellow powder (yield 86%), m.p. > 300 °C; ^{1}H NMR δ *ppm*: 3.24 (s, 3H, CH_3), 5.05 (s, 2H, *N*—CH_2), 7.04 (d, 1H, Ar—H, *J* = 7.5 Hz), 7.20 (t, 1H, Ar—H, *J* = 7.5 Hz), 7.31 (t, 1H, Ar—H, *J* = 8.0 Hz), 7.40–7.44 (m, 2H, Ar—H), 7.55 (t, 1H, Ar—H, *J* = 8.5 Hz), 7.69–7.76 (m, 4H, Ar—H), 7.90 (s, 1H, Ar—H), 8.09 (t, 1H, Ar—H, *J* = 7.5 Hz), 12.90 (s, 1H, NH of hydrazide spacer); ^{13}C NMR δ *ppm*: 14.17 (CH3), 41.83 (*N*-CH2), 110.23, 111.58, 112.79, 118.35, 118.59, 119.18, 121.08, 121.16, 123.40, 124.22, 125.54, 126.21, 129.71, 129.95, 130.75, 131.29, 131.63, 132.12, 134.35, 137.12, 138.24, 143.34, 148.33, 160.81 (C═O 2-indolinone), 171.63 (C═O hydrazide spacer); IR (KBr, ν cm^{-1}) 3358 (NH), 2210 (CN) and 1724, 1700 (2C═O); MS *m/z* [%]: 490 [M^+, 35.23], 102 [100]; Anal. Calcd. for $C_{27}H_{18}N_6O_2S$: C, 66.11; H, 3.70; N, 17.13; found C, 66.24; H, 3.66; N, 17.06; HPLC (t_{ret}) = 5.94 min (98.0% at 254 nm).

4.1.3.13. 6-Bromo-3-methyl-N'-(2-oxo-1-propylindolin-3-ylidene)benzo[4,5]imidazo[2,1-b]thiazole-2-carbohydrazide ***10h.*** Orange powder (yield 81%), m.p. 285–286 °C; ^{1}H NMR δ *ppm*: 0.90 (t, 3H, —CH_2—$\underline{CH_3}$, *J* = 7.5 Hz), 1.66–1.68 (m, 2H, —$\underline{CH_2}$—CH_3), 3.21 (s, 3H, CH_3), 3.71 (t, 2H, *N*—CH_2, *J* = 7.0 Hz), 7.20 (d, 1H, Ar—H, *J* = 8.0 Hz), 7.30 (t, 1H, Ar—H, *J* = 7.5 Hz), 7.40 (t, 1H, Ar—H, *J* = 7.5 Hz), 7.63 (d, 1H, Ar—H, *J* = 8.5 Hz), 7.70 (d, 1H, Ar—H, *J* = 8.5 Hz), 7.75 (s, 1H, Ar—H), 8.08 (d, 1H, Ar—H, *J* = 8.0 Hz), 12.92 (s, 1H, NH of hydrazide spacer); IR (KBr, ν cm^{-1}) 3335 (NH) and 1731, 1708 (2C═O); Anal. Calcd. for $C_{22}H_{18}BrN_5O_2S$: C, 53.23; H, 3.66; N, 14.11; found C, 53.09; H, 3.70; N, 14.15; HPLC (t_{ret}) = 4.87 min (97.1% at 254 nm).

4.1.3.14. N'-(1-Benzyl-2-oxoindolin-3-ylidene)-6-bromo-3-methylbenzo[4,5]imidazo[2,1-b]thiazole-2-carbohydrazide ***10i.*** Orange powder (yield 83%), m.p. >300 °C; ^{1}H NMR δ *ppm*: 3.21 (s, 3H, CH_3), 4.99 (s, 2H, *N*—CH_2), 6.99 (d, 1H, Ar—H, *J* = 8.0 Hz), 7.28–7.34 (m, 4H, Ar—H), 7.35–7.39 (m, 3H, Ar—H), 7.57 (d, 1H, Ar—H, *J* = 9.0 Hz), 7.69 (d, 1H, Ar—H, *J* = 8.0 Hz), 7.77 (s, 1H, Ar—H), 8.08 (d, 1H, Ar—H, *J* = 8.0 Hz), 11.99 (s, 1H, NH of hydrazide spacer); IR (KBr, ν cm^{-1}) 3330 (NH) and 1730, 1701 (2C═O); Anal. Calcd. for $C_{26}H_{18}BrN_5O_2S$: C, 57.36; H, 3.33; N, 12.86; found; C, 57.52; H, 3.29; N, 12.77; HPLC (t_{ret}) = 6.25 min (95.8% at 254 nm).

4.2. Biological evaluation

All experimental procedures utilized in the herein conducted biological assays were carried out as reported earlier; cytotoxicity [71], cell cycle [72], Annexin V-FITC Apoptosis [73,74] and CDK2 kinase [75] assays, and were provided in the Supplementary Materials.

4.3. In silico study

4.3.1. In silico ADME calculation

Swiss ADME server available online (http://www.swissadme.ch/index.php) was implemented to calculate the physicochemical properties for the three lead hybrids **7a**, **7d** and **10a**. The server relies on an accurate and efficient iLOG algorithm to calculate the physicochemical properties of small molecules [76]. The server gives plenty of data about the pharmacokinetic profiles of small molecules including detailed description of their absorption and metabolism. Another valuable data provided from the server is the drug-like nature [77].

4.3.2. Docking studies

The docking study was conducted by the freely available Vina Autodock software. Vina Autodock is more accurate and twice speed higher than Autodock 4 software [78]. Further speed-up is achieved from parallelism, using multithreading on multi-core machines. The crystal structure of CDK2 was obtained from the protein data bank PDB ID (4FX3). Before commencing the docking, CDK2 enzyme was energy minimized and equilibrated for 5 ns see Molecular dynamics section. Vina Autodock requires the receptor and the ligands in pdbqt format plus the coordinates and the size of a grid box surrounding the binding site. For that, M.G.L tools were used to prepare the needed files in the right format besides, generating a grid box surrounding the binding site of the co-crystalized ligand with CDK2 enzyme [79]. Then, the docking study was conducted at two steps. Firstly, the co-crystalized ligand was re-docked to its corresponding enzyme once in water presence and another time in water absence to ensure validity of the docking protocol. Finally, the three synthesized lead hybrids were docked into CDK2 enzyme. The docking results were visualized by Biovia discovery studio 2020 free visualizer (https://3dsbiovia.com/resource-center/downloads/) that was used to generate 2D and 3D interactions for the docked compounds.

4.3.3. Molecular dynamics

To support the docking results, we performed three molecular dynamic simulations experiments. The three experiments were for CDK2 enzyme in complex with the three lead compounds. The latest version of GROningen MAchine for Chemical Simulations (GROMACS 2020.3) was implemented to conduct the three MD simulation experiments [80]. The receptor topology was obtained by the 'pdb2gmx' script, and CHARMM General Force Field (CGENFF) server was used to generate the receptor and ligand topologies, respectively [81]. The ligand topologies were

then converted to the gromacs format using the 'cgenff_charmm2gmx_py3_nx2.py' script. Each of the three generated ligand topologies was rejoined to the processed receptor structure to construct the ligand–protein complex. Then, all the systems were solvated with a single point charge (SPC) water model to add water molecules to the cubic simulation boxes. 'gmx genion' script was used to neutralize the system net charges by adding counter-ions. Energy minimization of the receptor and the processed complexes was performed under GROMOS96 43a1 force field [82] by employing a steepest descent minimization algorithm with a maximum of 50,000 steps and >10.0 kJ/mol force. Then, the solvated energy minimized structures were equilibrated for two consecutive steps. Firstly, NVT ensemble with constant number of particles, volume and temperature was done for 1 ns followed by NPT ensemble with constant number of particles, pressure and temperature for 4 ns. In the two steps of equilibration, only the solvent molecules were allowed for free movement to ensure its equilibration in the system while other atoms were restrained. The long range electrostatic interactions were obtained by the particle mesh Ewald method with a 12 Å cut-off and 12 Å Fourier spacing [83]. Finally, the four equilibrated systems (one empty enzyme and three protein–ligand complexes) were then entered the production stage without any restrains for 100 ns with a time step of 2 fs, and after every 5 ps the structural coordinates were saved. The root mean square deviation (RMSD) was calculated from the generated trajectories of the MD simulations as well as the distances of the formed hydrogen bonds between the receptor and the ligands by various built-in scripts of GROMACS.

4.3.4. MM-PBSA calculation

A very important data retrieved from MD simulations and thermodynamic calculations is the determination of the binding free energy of a protein–ligand complex. According to the following equation: $\Delta G_{(Binding)} = G_{(Complex)} - G_{(Receptor)} - G_{(Ligand)}$

The binding free energy of protein and ligand complexes can be calculated using the molecular Mechanic/ Poisson-Boltzmann Surface Area (MM-PBSA) alongside MD simulations Where, G (complex) is the total free energy of the protein–ligand complex and G (receptor) and G (ligand) are total free energies of the isolated protein and ligand in solvent, respectively. The total free energy of any of the three mentioned systems (complex or receptor or ligand) are the sum of its molecular mechanics potential energy plus the solvation energy. The 'g_mmpbsa' package of GROMACS was used perform MM-PBSA calculations through all the MD trajectories [67].

Declaration of Competing Interest

The authors declare that they have no known competing financial interests or personal relationships that could have appeared to influence the work reported in this paper.

Acknowledgement

The authors acknowledge financial support from the Researchers Supporting Project number (RSP-2020/103), King Saud University, Riyadh, Saudi Arabia. Also, this research was funded by the Deanship of Scientific Research at Princess Nourah bint Abdulrahman University through the Fast-track Research Funding Program.

Appendix A. Supplementary material

Supplementary data to this article can be found online at https://doi.org/10.1016/j.bioorg.2021.104748.

References

[1] R.L. Siegel, K.D. Miller, A. Jemal, Cancer statistics, 2016, CA Cancer J. Clin. 66 (2016) 7–30.
[2] R.L. Siegel, K.D. Miller, A. Jemal, Cancer statistics, 2020, CA Cancer J. Clin. 70 (2020) 7–30.
[3] K. Cheung-Ong, G. Giaever, C. Nislow, DNA-damaging agents in cancer chemotherapy: serendipity and chemical biology, Chem. Biol. 20 (2013) 648–659.
[4] P.L. Fischhaber, A.S. Gall, J.A. Duncan, P.B. Hopkins, Direct demonstration in synthetic oligonucleotides that N, N'-bis(2-chloroethyl)-nitrosourea cross links N1 of deoxyguanosine to N3 of deoxycytidine on opposite strands of duplex DNA, Cancer Res. 59 (1999) 4363–4368.
[5] L.S. Goodman, M.M. Wintrobe, Nitrogen mustard therapy; use of methyl-bis (beta-chloroethyl) amine hydrochloride and tris (beta-chloroethyl) amine hydrochloride for Hodgkin's disease, lymphosarcoma, leukemia and certain allied and miscellaneous disorders, J. Am. Med. Assoc. 132 (1946) 126–132.
[6] S. Farber, L.K. Diamond, Temporary remissions in acute leukemia in children produced by folic acid antagonist, 4-aminopteroyl-glutamic acid, N. Engl. J. Med. 238 (1948) 787–793.
[7] J.L. Nitiss, DNA topoisomerases in cancer chemotherapy: using enzymes to generate selective DNA damage, Curr. Opin. Investig. Drugs 3 (2002) 1512–1516.
[8] J.L. Nitiss, Targeting DNA topoisomerase II in cancer chemotherapy, Nat. Rev. Cancer 9 (2009) 338–350.
[9] S. Wadler, J.Z. Fuks, P.H. Wiernik, Phase I and II agents in cancer therapy: I. Anthracyclines and related compounds, J. Clin. Pharmacol. 26 (1986) 491–509.
[10] V.T. DeVita Jr., E. Chu, A history of cancer chemotherapy, Cancer Res. 68 (2008) 8643–8653.
[11] E. Espinosa, P. Zamora, J. Feliu, M. Gonzalez Baron, Classification of anticancer drugs-a new system based on therapeutic targets, Cancer Treat. Rev. 29 (2003) 515–523.
[12] B. Mansoori, A. Mohammadi, S. Davudian, S. Shirjang, B. Baradaran, The different mechanisms of cancer drug resistance: a brief review, Adv. Pharm. Bull. 7 (2017) 339–348.
[13] T.A. Baudino, Targeted cancer therapy: the next generation of cancer treatment, Curr. Drug Discov. Technol. 12 (2015) 3–20.
[14] P. Cohen, Protein kinases–the major drug targets of the twenty-first century? Nat. Rev. Drug Discov. 1 (2002) 309–315.
[15] R. Santos, O. Ursu, A. Gaulton, A.P. Bento, R.S. Donadi, C.G. Bologa, A. Karlsson, B. Al-Lazikani, A. Hersey, T.I. Oprea, J.P. Overington, A comprehensive map of molecular drug targets, Nat. Rev. Drug Discov. 16 (2017) 19–34.
[16] S. Lapenna, A. Giordano, Cell cycle kinases as therapeutic targets for cancer, Nat. Rev. Drug Discov. 8 (2009) 547–566.
[17] C. Sanchez-Martinez, L.M. Gelbert, M.J. Lallena, A. de Dios, Cyclin dependent kinase (CDK) inhibitors as anticancer drugs, Bioorg. Med. Chem. Lett. 25 (2015) 3420–3435.
[18] U. Asghar, A.K. Witkiewicz, N.C. Turner, E.S. Knudsen, The history and future of targeting cyclin-dependent kinases in cancer therapy, Nat. Rev. Drug Discov. 14 (2015) 130–146.
[19] R.M. Golsteyn, Cdk1 and Cdk2 complexes (cyclin dependent kinases) in apoptosis: a role beyond the cell cycle, Cancer Lett. 217 (2005) 129–138.
[20] X. Grana, E.P. Reddy, Cell cycle control in mammalian cells: role of cyclins, cyclin dependent kinases (CDKs), growth suppressor genes and cyclin-dependent kinase inhibitors (CKIs), Oncogene 11 (1995) 211–219.
[21] D.O. Morgan, Principles of CDK regulation, Nature 374 (1995) 131–134.
[22] C.J. Sherr, Cancer cell cycles, Science 274 (1996) 1672–1677.
[23] D. Horiuchi, N.E. Huskey, L. Kusdra, L. Wohlbold, K.A. Merrick, C. Zhang, K. J. Creasman, K.M. Shokat, R.P. Fisher, A. Goga, Chemical-genetic analysis of cyclin dependent kinase 2 function reveals an important role in cellular transformation by multiple oncogenic pathways, Proc. Natl. Acad. Sci. U S A 109 (2012) 1019–1027.
[24] J.J. Molenaar, M.E. Ebus, D. Geerts, J. Koster, F. Lamers, L.J. Valentijn, E. M. Westerhout, R. Versteeg, H.N. Caron, Inactivation of CDK2 is synthetically lethal to MYCN over-expressing cancer cells, Proc. Natl. Acad. Sci. U S A 106 (2009) 12968–12973.
[25] A.J. Deans, K.K. Khanna, C.J. McNees, C. Mercurio, J. Heierhorst, G.A. McArthur, Cyclin-dependent kinase 2 functions in normal DNA repair and is a therapeutic target in BRCA1-deficient cancers, Cancer Res. 66 (2006) 8219–8226.
[26] M.K. Abd El Hamid, M.D. Mihovilovic, H.B. El-Nassan, Synthesis of novel pyrazolo [3,4-d]pyrimidine derivatives as potential anti-breast cancer agents, Eur. J. Med. Chem. 57 (2012) 323–328.
[27] T. Otto, P. Sicinski, Cell cycle proteins as promising targets in cancer therapy, Nat. Rev. Cancer 17 (2017) 93–115.
[28] S.R. Whittaker, A. Mallinger, P. Workman, P.A. Clarke, Inhibitors of cyclin-dependent kinases as cancer therapeutics, Pharmacol. Ther. 173 (2017) 83–105.
[29] H. Guo, Isatin derivatives and their anti-bacterial activities, Eur. J. Med. Chem. 164 (2019) 678–688.
[30] G. Mathur, S. Nain, Recent advancement in synthesis of isatin as anticonvulsant agents, a review, Med. Chem. 4 (2014) 417–427.
[31] A. Medvedev, O. Buneeva, O. Gnedenko, P. Ershov, A. Ivanov, Isatin, an endogenous nonpeptide biofactor: a review of its molecular targets, mechanisms of actions, and their biomedical implications, Biofactors 44 (2018) 95–108.
[32] P. Phogat, P. Singh, A mini review on central nervous system potential of isatin derivatives, Cent. Nerv. Syst. Agents Med. Chem. 15 (2015) 28–31.
[33] R.A. Rane, S. Karunanidhi, K. Jain, M. Shaikh, G. Hampannavar, R. Karpoormath, A recent perspective on discovery and development of diverse therapeutic agents inspired from isatin alkaloids, Curr. Top. Med. Chem. 16 (2016) 1262–1289.
[34] A. Singh, J.V. Singh, A. Rana, K. Bhagat, H.K. Gulati, R. Kumar, R. Salwan, G. Kaur, N. Singh, H. Singh, S. Sharma, P.M.S. Bedi, Monocarbonyl curcumin-based molecular hybrids as potent antibacterial agents, ACS Omega 4 (2019) 11673–11684.
[35] K. Bhagat, J. Bhagat, M.K. Gupta, J.V. Singh, H.K. Gulati, A. Singh, K. Kaur, G. Kaur, S. Sharma, A. Rana, H. Singh, P.M. Singh Bedi, Design, synthesis,

antimicrobial evaluation, and molecular modeling studies of novel indolinedione-coumarin molecular hybrids, ACS Omega 4 (2019) 8720–8730.
[36] H. Singh, J.V. Singh, M.K. Gupta, A.K. Saxena, S. Sharma, K. Nepali, P.M.S. Bedi, Triazole tethered isatin-coumarin based molecular hybrids as novel antitubulin agents: design, synthesis, biological investigation and docking studies, Bioorg. Med. Chem. Lett. 27 (2017) 3974–3979.
[37] H.A. Abdel-Aziz, H.A. Ghabbour, W.M. Eldehna, M.M. Qabeel, H.K. Fun, Synthesis, crystal structure, and biological activity of cis/trans amide rotomers of (Z)-N′-(2-oxoindolin-3-ylidene) formohydrazide, J. Chem. 2 (2014) 1–7.
[38] M.F. Abo-Ashour, W.M. Eldehna, R.F. George, M.M. Abdel-Aziz, M.M. Elaasser, N. M. Abdel Gawad, A. Gupta, S. Bhakta, S.M. Abou-Seri, Novel indole-thiazolidinone conjugates: Design, synthesis and whole-cell phenotypic evaluation as a novel class of antimicrobial agents, Eur. J. Med. Chem. 160 (2018) 49–60.
[39] Z. Ding, M. Zhou, C. Zeng, Recent advances in isatin hybrids as potential anticancer agents, Arch Pharm (Weinheim) 353 (2020), e1900367.
[40] A.K. Gupta, S. Tulsyan, M. Bharadwaj, R. Mehrotra, Systematic review on cytotoxic and anticancer potential of N-substituted isatins as novel class of compounds useful in multidrug-resistant cancer therapy: in silico and in vitro analysis, Top Curr. Chem. (Cham) 377 (2019) 15.
[41] Y. Hou, C. Shang, H. Wang, J. Yun, Isatin-azole hybrids and their anticancer activities, Arch. Pharm. (Weinheim) 353 (2019), e1900272.
[42] S. Varun, S. Sonam, R. Kakkar, Isatin and its derivatives: a survey of recent syntheses, reactions, and applications, Med. Chem. Commun. 10 (2019) 351–368.
[43] H.N. Bramson, J. Corona, S.T. Davis, S.H. Dickerson, M. Edelstein, S.V. Frye, R. T. Gampe Jr., P.A. Harris, A. Hassell, W.D. Holmes, R.N. Hunter, K.E. Lackey, B. Lovejoy, M.J. Luzzio, V. Montana, W.J. Rocque, D. Rusnak, L. Shewchuk, J. M. Veal, D.H. Walker, L.F. Kuyper, Oxindole-based inhibitors of cyclin-dependent kinase 2 (CDK2): design, synthesis, enzymatic activities, and X-ray crystallographic analysis, J. Med. Chem. 44 (2001) 4339–4358.
[44] H.E. Dweedar, H. Mahrous, H.S. Ibrahim, H.A. Abdel-Aziz, Analogue-based design, synthesis and biological evaluation of 3-substituted-(methylenehydrazono)indolin-2-ones as anticancer agents, Eur. J. Med. Chem. 78 (2014) 275–280.
[45] H.A. Abdel-Aziz, W.M. Eldehna, A.B. Keeton, G.A. Piazza, A.A. Kadi, M.W. Attwa, A.S. Abdelhameed, M.I. Attia, Isatin-benzoazine molecular hybrids as potential antiproliferative agents: synthesis and in vitro pharmacological profiling, Drug Des. Devel. Ther. 11 (2017) 2333–2346.
[46] M.I. Attia, W.M. Eldehna, S.A. Afifi, A.B. Keeton, G.A. Piazza, H.A. Abdel-Aziz, New hydrazonoindolin-2-ones: Synthesis, exploration of the possible anti-proliferative mechanism of action and encapsulation into PLGA microspheres, PLoS One 12 (2017), e0181241.
[47] W.M. Eldehna, R.I. Al-Wabli, M.S. Almutairi, A.B. Keeton, G.A. Piazza, H.A. Abdel-Aziz, M.I. Attia, Synthesis and biological evaluation of certain hydrazonoindolin-2-one derivatives as new potent anti-proliferative agents, J. Enzy. Inhib. Med. Chem. 33 (2018) 867–878.
[48] T. Al-Warhi, M.F. Abo-Ashour, H. Almahli, O.J. Alotaibi, M.M. Al-Sanea, G.H. Al-Ansary, H.Y. Ahmed, M.M. Elaasser, W.M. Eldehna, H.A. Abdel-Aziz, Novel [(N-alkyl-3-indolylmethylene)hydrazono]oxindoles arrest cell cycle and induce cell apoptosis by inhibiting CDK2 and Bcl-2: synthesis, biological evaluation and in silico studies, J. Enzy. Inhib. Med. Chem. 35 (2020) 1300–1309.
[49] T. Al-Warhi, A.M. El Kerdawy, N. Aljaeed, O.E. Ismael, R.R. Ayyad, W.M. Eldehna, H.A. Abdel-Aziz, G.H. Al-Ansary, Synthesis, biological evaluation and in silico studies of certain oxindole-indole conjugates as anticancer CDK inhibitors, Molecules 25 (2020) 2031–2050.
[50] W.M. Eldehna, G.S. Hassan, S.T. Al-Rashood, H.M. Alkahtani, A.A. A, G.H. Al-Ansary, Marine-inspired bis-indoles possessing antiproliferative activity against breast cancer; design, synthesis, and biological evaluation, Mar. Drugs 18 (2020) 190–205.
[51] G.H. Al-Ansary, W.M. Eldehna, H.A. Ghabbour, S.T.A. Al-Rashood, K.A. Al-Rashood, R.A. Eladwy, A. Al-Dhfyan, M.M. Kabil, H.A. Abdel-Aziz, Cancer stem cells CD133 inhibition and cytotoxicity of certain 3-phenylthiazolo[3,2-a]benzimidazoles: design, direct synthesis, crystal study and in vitro biological evaluation, J. Enzy. Inhib. Med. Chem. 32 (2017) 986–991.
[52] M.M. El-Kerdawy, M.A. Ghaly, S.A. Darwish, H.A. Abdel-Aziz, A.R. Elsheakh, R. S. Abdelrahman, G.S. Hassan, New benzimidazothiazole derivatives as anti-inflammatory, antitumor active agents: synthesis, in-vitro and in-vivo screening and molecular modeling studies, Bioorg. Chem. 83 (2019) 250–261.
[53] M. El-Naggar, W.M. Eldehna, H. Almahli, A. Elgez, M. Fares, M.M. Elaasser, H. A. Abdel-Aziz, Novel Thiazolidinone/Thiazolo[3,2-a]Benzimidazolone-Isatin conjugates as apoptotic anti-proliferative agents towards breast cancer: one-pot synthesis and in vitro biological evaluation, Molecules 23 (2018) 1420.
[54] Y. Li, J. Zhang, W. Gao, L. Zhang, Y. Pan, S. Zhang, Y. Wang, Insights on structural characteristics and ligand binding mechanisms of CDK2, Int. J. Mol. Sci. 16 (2015) 9314–9340.
[55] P. Skehan, R. Storeng, D. Scudiero, A. Monks, J. McMahon, D. Vistica, J.T. Warren, H. Bokesch, S. Kenney, M.R. Boyd, New colorimetric cytotoxicity assay for anticancer-drug screening, J. Natl. Cancer Inst. 82 (1990) 1107–1112.
[56] V. Nikoletopoulou, M. Markaki, K. Palikaras, N. Tavernarakis, Crosstalk between apoptosis, necrosis and autophagy, Biochim. Biophys. Acta 2013 (1833) 3448–3459.
[57] F. Radogna, M. Dicato, M. Diederich, Cancer-type-specific crosstalk between autophagy, necroptosis and apoptosis as a pharmacological target, Biochem. Pharmacol. 94 (2015) 1–11.
[58] Z. Su, Z. Yang, Y. Xu, Y. Chen, Q. Yu, Apoptosis, autophagy, necroptosis, and cancer metastasis, Mol. Cancer 14 (2015) 48–61.
[59] S. Kasibhatla, B. Tseng, Why target apoptosis in cancer treatment? Mol. Cancer Ther. 2 (2003) 573–580.
[60] A. Daina, V. Zoete, A BOILED-egg to predict gastrointestinal absorption and brain penetration of small molecules, ChemMedChem 11 (2016) 1117–1121.
[61] J.B. Baell, G.A. Holloway, New substructure filters for removal of pan assay interference compounds (PAINS) from screening libraries and for their exclusion in bioassays, J. Med. Chem. 53 (2010) 2719–2740.
[62] D.F. Veber, S.R. Johnson, H.Y. Cheng, B.R. Smith, K.W. Ward, K.D. Kopple, Molecular properties that influence the oral bioavailability of drug candidates, J. Med. Chem. 45 (2002) 2615–2623.
[63] Y. Wei, J. Li, J. Qing, M. Huang, M. Wu, F. Gao, D. Li, Z. Hong, L. Kong, W. Huang, J. Lin, Discovery of novel hepatitis C virus NS5B polymerase inhibitors by combining random forest, multiple e-pharmacophore modeling and docking, PLoS One 11 (2016), e0148181.
[64] M.A.E. El-Hasab, E.E. El-Bastawissy, T.F. El-Moselhy, Identification of potential inhibitors for HCV NS3 genotype 4a by combining protein-ligand interaction fingerprint, 3D pharmacophore, docking, and dynamic simulation, J. Biomol. Struct. Dyn. 36 (2018) 1713–1727.
[65] M.A.E. El-Hassab, E.E. El-Bastawissy, T.F. El-Moselhy, Identification of potential inhibitors for HCV NS5b of genotype 4a by combining dynamic simulation, protein-ligand interaction fingerprint, 3D pharmacophore, docking and 3D QSAR, J. Biomol. Struct. Dyn. 6 (2019) 1–15.
[66] H. Nagarajan, S. Narayanaswamy, U. Vetrivel, Mutational landscape screening of methylene tetrahydrofolate reductase to predict homocystinuria associated variants: an integrative computational approach, Mutat. Res. 819–820 (2020), 111687.
[67] A. Daina, O. Michielin, V. Zoete, iLOGP: a simple, robust, and efficient description of n-octanol/water partition coefficient for drug design using the GB/SA approach, J. Chem. Inf. Model. 54 (2014) 3284–3301.
[68] H.A. Abdel-Aziz, N.A. Hamdy, A.M. Farag, I.M.I. Fakhr, Synthesis and reactions of 3-methylthiazolo [3,2-a] benzimidazole-2-carboxylic acid hydrazide: synthesis of some new pyrazole, 1,3-thiazoline, 1,2,4-triazole and 1,2,4-triazolo [3,4-b]-1,3,4-thiadiazine derivatives pendant to thiazolo [3,2-a] benzimidazole moiety, J. Chin. Chem. Soc. 54 (2007) 1573–1582.
[69] A.A.M. Alkhaldi, M.M. Al-Sanea, A. Nocentini, W.M. Eldehna, Z.M. Elsayed, A. Bonardi, M.F. Abo-Ashour, A.K. El-Damasy, M.S. Abdel-Maksoud, T. Al-Warhi, P. Gratteri, H.A. Abdel-Aziz, C.T. Supuran, R. El-Haggar, 3-Methylthiazolo[3,2-a] benzimidazole-benzenesulfonamide conjugates as novel carbonic anhydrase inhibitors endowed with anticancer activity: design, synthesis, biological and molecular modeling studies, Eur. J. Med. Chem. (2020) In press.
[70] W.M. Eldehna, M. Fares, H.S. Ibrahim, M.A. Alsherbiny, M.H. Aly, H.A. Ghabbour, H.A. Abdel-Aziz, Synthesis and cytotoxic activity of biphenylurea derivatives containing indolin-2-one moieties, Molecules 21 (2016) 762.
[71] A. Sabt, O.M. Abdelhafez, R.S. El-Haggar, H.M.F. Madkour, W.M. Eldehna, E. El-Khrisy, M.A. Abdel-Rahman, L.A. Rashed, Novel coumarin-6-sulfonamides as apoptotic anti-proliferative agents: synthesis, in vitro biological evaluation, and QSAR studies, J. Enzy. Inhib. Med. Chem. 33 (2018) 1095–1107.
[72] H.A. Mahdy, M.K. Ibrahim, A.M. Metwaly, A. Belal, A.B.M. Mehany, K.M.A. El-Gamal, A. El-Sharkawy, M.A. Elhendawy, M.M. Radwan, M.A. Elsohly, I.H. Eissa, Design, synthesis, molecular modeling, in vivo studies and anticancer evaluation of quinazolin-4(3H)-one derivatives as potential VEGFR-2 inhibitors and apoptosis inducers, Bioorg. Chem. 94 (2020), 103422.
[73] W.M. Eldehna, G.S. Hassan, S.T. Al-Rashood, T. Al-Warhi, A.E. Altyar, H. M. Alkahtani, A.A. Almehizia, H.A. Abdel-Aziz, Synthesis and in vitro anticancer activity of certain novel 1-(2-methyl-6-arylpyridin-3-yl)-3-phenylureas as apoptosis-inducing agents, J. Enzy. Inhib. Med. Chem. 34 (2019) 322–332.
[74] S.A. Elmetwally, K.F. Saied, I.H. Eissa, E.B. Elkaeed, Design, synthesis and anticancer evaluation of thieno[2,3-d]pyrimidine derivatives as dual EGFR/HER2 inhibitors and apoptosis inducers, Bioorg. Chem. 88 (2019), 102944.
[75] A. Sabt, W.M. Eldehna, T. Al-Warhi, O.J. Alotaibi, M.M. Elaasser, H. Suliman, H. A. Abdel-Aziz, Discovery of 3,6-disubstituted pyridazines as a novel class of anticancer agents targeting cyclin-dependent kinase 2: synthesis, biological evaluation and in silico insights, J. Enzy. Inhib. Med. Chem. 35 (2020) 1616–1630.
[76] A. Daina, O. Michielin, V. Zoete, SwissADME: a free web tool to evaluate pharmacokinetics, drug-likeness and medicinal chemistry friendliness of small molecules, Sci. Rep. 7 (2017) 42717.
[77] O. Trott, A.J. Olson, AutoDock Vina: improving the speed and accuracy of docking with a new scoring function, efficient optimization, and multithreading, J. Comput. Chem. 31 (2010) 455–461.
[78] P. Ayaz, D. Andres, D.A. Kwiatkowski, C.C. Kolbe, P. Lienau, G. Siemeister, U. Lucking, C.M. Stegmann, Conformational adaption may explain the slow dissociation kinetics of roniciclib (BAY 1000394), a type I CDK inhibitor with kinetic selectivity for CDK2 and CDK9, ACS Chem. Biol. 11 (2016) 1710–1719.
[79] M.J. Abraham, T. Murtola, R. Schulz, S. Pall, J.C. Smith, B. Hess, E. Lindahl, GROMACS: High performance molecular simulations through multi-level parallelism from laptops to supercomputers, SoftwareX 1–2 (2015) 19–25.
[80] J.C. Phillips, R. Braun, W. Wang, J. Gumbart, E. Tajkhorshid, E. Villa, C. Chipot, R. D. Skeel, L. Kale, K. Schulten, Scalable molecular dynamics with NAMD, J. Comput. Chem. 26 (2005) 1781–1802.
[81] S.W. Chiu, S.A. Pandit, H.L. Scott, E. Jakobsson, An improved united atom force field for simulation of mixed lipid bilayers, J. Phys. Chem. B 113 (2009) 2748–2763.
[82] V.K. Bhardwaj, R. Singh, J. Sharma, V. Rajendran, R. Purohit, S. Kumar, Identification of bioactive molecules from tea plant as SARS-CoV-2 main protease inhibitors, J. Biomol. Struct. Dyn. 20 (2020) 1–10.
[83] R. Kumari, R. Kumar, A. Lynn, g_mmpbsa–a GROMACS tool for high-throughput MM-PBSA calculations, J. Chem. Inf. Model. 54 (2014) 1951–1962.